Monthly Notices
of the
ROYAL ASTRONOMICAL SOCIETY

MNRAS **476,** 3611–3630 (2018)
Advance Access publication 2018 February 22

doi:10.1093/mnras/sty478

SN 2015as: a low-luminosity Type IIb supernova without an early light-curve peak

Anjasha Gangopadhyay,[1,2★] Kuntal Misra,[1★] A. Pastorello,[3★] D. K. Sahu,[4] L. Tomasella,[3] L. Tartaglia,[3] Mridweeka Singh,[1,2] Raya Dastidar,[1,5] S. Srivastav,[4] P. Ochner,[3] Peter J. Brown,[6] G. C. Anupama,[4] S. Benetti,[3] E. Cappellaro,[3] Brajesh Kumar,[4] Brijesh Kumar[1] and S. B. Pandey[1]

[1]*Aryabhatta Research Institute of Observational Sciences, Manora Peak, Nainital 263 002, India*
[2]*School of Studies in Physics and Astrophysics, Pandit Ravishankar Shukla University, Chattisgarh 492 010, India*
[3]*INAF Osservatorio Astronomico di Padova, Vicolo dell'Osservatorio 5, I-35122 Padova, Italy*
[4]*Indian Institute of Astrophysics, Koramangala, Bangalore 560 034, India*
[5]*Department of Physics & Astrophysics, University of Delhi, Delhi 110 007, India*
[6]*Department of Physics and Astronomy, George P. and Cynthia Woods Mitchell Institute for Fundamental Physics & Astronomy, Texas A&M University, 4242 TAMU, College Station, TX 77843, USA*

Accepted 2018 February 16. Received 2018 February 13; in original form 2017 July 13

ABSTRACT

We present results of the photometric (from 3 to 509 d post-explosion) and spectroscopic (up to 230 d post-explosion) monitoring campaign of the He-rich Type IIb supernova (SN) 2015as. The $(B - V)$ colour evolution of SN 2015as closely resemble those of SN 2008ax, suggesting that SN 2015as belongs to the SN IIb subgroup that does not show the early, short-duration photometric peak. The light curve of SN 2015as reaches the B-band maximum about 22 d after the explosion, at an absolute magnitude of -16.82 ± 0.18 mag. At ∼75 d after the explosion, its spectrum transitions from that of a SN II to a SN Ib. P Cygni features due to He I lines appear at around 30 d after explosion, indicating that the progenitor of SN 2015as was partially stripped. For SN 2015as, we estimate a ^{56}Ni mass of ∼0.08 $M_\odot$ and ejecta mass of 1.1–2.2 $M_\odot$, which are similar to the values inferred for SN 2008ax. The quasi-bolometric analytical light-curve modelling suggests that the progenitor of SN 2015as has a modest mass (∼0.1 $M_\odot$), a nearly compact ($\sim 0.05 \times 10^{13}$ cm) H envelope on top of a dense, compact ($\sim 2 \times 10^{11}$ cm) and a more massive (∼1.2 $M_\odot$) He core. The analysis of the nebular phase spectra indicates that ∼0.44 $M_\odot$ of O is ejected in the explosion. The intensity ratio of the [Ca II]/[O I] nebular lines favours either a main-sequence progenitor mass of ∼15 $M_\odot$ or a Wolf–Rayet star of 20 $M_\odot$.

Key words: techniques: photometric – techniques: spectroscopic – supernovae: general – supernovae: individual: SN 2015as – galaxies: individual: UGC 5460.

1 INTRODUCTION

Supernovae of Type IIb (SNe IIb) are transitional objects whose spectra are dominated by hydrogen (H) lines at early phases, similar to Type II SNe. However, at later phases, their spectra share similarity with Type Ib SNe, being dominated by emerging helium (He) lines. The hydrogen-deficient core-collapse SNe are designated as Type Ib or Ic based on the presence or absence of helium features near about maximum light. SNe IIb, Ib, and Ic are collectively known as stripped-envelope SNe. SNe IIb are limited in number, but they provide an interesting link between H-rich and H-poor core-collapse SNe. In a volume-limited sample consisting of 81 Type II SNe, Li et al. (2011) found that Type IIb events are $11.9^{+3.9}_{-3.6}$ per cent. In a recent study by Shivvers et al. (2017), stripped-envelope SNe constitute ∼10 per cent among core-collapse SNe. Well studied SNe IIb include SN 1987K (Filippenko 1988), SN 1993J (Filippenko, Matheson & Ho 1993; Aldering, Humphreys & Richmond 1994; Baron, Hauschildt & Branch 1994; Barbon et al. 1995; Richmond et al. 1996; Matheson et al. 2000b; Filippenko & Matheson 2003; Jerkstrand et al. 2015), SN 1996cb (Qiu et al. 1999; Deng et al. 2001), SN 2001ig (Ryder, Murrowood & Stathakis 2006), SN 2003bg (Hamuy et al. 2009; Mazzali et al. 2009), SN

★ E-mail: anjasha@aries.res.in, anjashagangopadhyay@gmail.com (AG); kuntal@aries.res.in (KM); andrea.pastorello@oapd.inaf.it (AP)

2008ax (Pastorello et al. 2008; Chornock et al. 2011; Taubenberger et al. 2011), SN 2009mg (Oates et al. 2012), SN 2010as (Folatelli et al. 2014a), SN 2011dh (Arcavi et al. 2011; Sahu, Anupama & Chakradhari 2013; Ergon et al. 2015), SN 2011ei (Milisavljevic et al. 2013), SN 2011fu (Kumar et al. 2013; Morales-Garoffolo et al. 2015), SN 2011hs (Bufano et al. 2014), and SN 2013df (Morales-Garoffolo et al. 2014).

A fraction of SNe IIb (e.g. SNe 1993J,2011fu and 2013df) show two peaks in their light curve, while other objects such as SNe 1996cb and 2008ax show only the broad maximum. The initial peak (observed in ∼50 per cent of SNe IIb, according to Morales-Garoffolo (2016)), is interpreted as a signature of the rapid cooling phase after the shock breakout, and lasts from seconds to days (Morales-Garoffolo 2016). Thus, it can easily remain unobserved if the shock breakout occurs in a low-density shell. The rapid decline phase is due to adiabatic cooling, and its duration depends primarily on the progenitor's size. The secondary peak is governed by the thermalization of γ-rays and positrons during the radioactive decay of ^{56}Ni → ^{56}Co → ^{56}Fe (Colgate 1970; Burger, Stephens & Swanenburg 1970). The peak luminosities of most SNe IIb indicate that 0.02–0.1 $M_\odot$ of ^{56}Ni is typically ejected during these explosions (Cano 2013; Prentice et al. 2016).

SNe IIb have unique spectroscopic features intermediate between those of Type II and Type I events. Because SN IIb spectra show H features at early phases which diminish over time while He features appear and strengthen, extended spectral sequences are essential to properly classify these transitional objects. Recent studies have claimed for the presence of some H in SNe Ib (Anupama et al. 2005; Parrent et al. 2007, 2016). A number of methods are used to draw a line between SNe IIb and Ib, including the estimate of the pseudo-equivalent width of the Hα line profile (Liu & Modjaz 2016), evaluating the ratio of the He I λ 5876 to Hα equivalent widths (Milisavljevic et al. 2013), and through a comparison of the observed spectrum with Type IIb/Ib templates (Parrent et al. 2016).

In SNe IIb, strong stellar winds in single massive stars or mass outflows due to binary interaction may contribute to strip the outer stellar envelope of the progenitor. Type IIb can have compact (cIIb, with $R \sim 10^{11}$ cm) or extended (eIIb, with $R \sim 10^{13}$ cm) progenitors. Chevalier & Soderberg (2010) find similar properties of the radio light curve for IIb SNe that have been associated by other means with a compact/extended progenitor. They were the first to attempt a separation in extended and compact IIbs based on radio observations. Their observations indicated compact progenitors for SNe 1996cb, 2001ig, and 2008ax, while those of SNe 1993J and 2001gd are extended. However, more recent studies (Bufano et al. 2014; Romero-Cañizales et al. 2014) claim that the inferred radio properties of a SN do not properly reflect the progenitor size.

Despite the small number of SNe IIb, direct detection for progenitors of four objects have been claimed. The progenitors were either Wolf–Rayet stars with $M_{\rm ZAMS}$ = 10–28 $M_\odot$ in a binary system, like in the case of SN 2008ax (Pastorello et al. 2008; Crockett et al. 2008), or more extended yellow supergiants with $M_{\rm ZAMS}$ = 12–17 $M_\odot$ like in SNe 2011dh and 2013df (Maund et al. 2011, 2015; Folatelli et al. 2014b; Van Dyk et al. 2011, 2013, 2014; Bersten et al. 2012). For SN 1993J, the inferred progenitor was a K0Ia star in a binary system, with an early B-Type supergiant companion (Filippenko et al. 1993; Aldering et al. 1994; Maund & Smartt 2009). Indirect indicators, such as the early-time light curves, spectral studies of light echos and/or signatures of CSM-ejecta interaction, may also help constraining the progenitor mass like in the case of SNe 2001ig and 2013df (Krause et al. 2008; Kamble et al. 2016). The early UV excess, for example, provides a method to estimate the progenitor radius (Ben-Ami et al. 2015). In the case of SN 2001ig, both the radio light curves and the spectro-polarimetric observations support the binary progenitor (Ryder et al. 2004; Maund et al. 2007), including a massive 10–18 $M_\odot$ Wolf–Rayet star (Ryder et al. 2006). According to an alternative interpretation given by Kotak & Vink (2006), the modulated late-time radio light curves would be a signature of a previous LBV-like pulsational phases.

In this paper, we present a photometric and spectroscopic study of the Type IIb SN 2015as. We provide information on the SN discovery and its host galaxy in Section 2. In Section 3, we describe the data acquisition and reduction procedures. In Section 4, we study the multiband light curves, and compare the colours, absolute light curves and bolometric evolution with those of other SNe IIb. The main explosion parameters are also computed through a basic analytical modelling of the bolometric light curve. The detailed description of the spectral evolution is presented in Section 5, while in Section 6 a summary of the main results of this study is given.

2 SN 2015AS AND ITS DISTANCE

SN 2015as was discovered by Ken'ichi Nishimura[1] on three unfiltered CCD exposures taken on 2015 November 15.778 UT with a 35 cm reflector. The SN is located at RA = $10^{\rm h}\ 08^{\rm m}\ 11\overset{\rm s}{.}37$ and Dec. = +51°50′40.9″, which is 19.″2 east and 2.″9 north of the centre of the SB(rs)d-Type host galaxy UGC 5460, which also hosted the Type IIn SN 2011ht (Humphreys et al. 2012; Roming et al. 2012; Fraser et al. 2013; Mauerhan et al. 2013). The unfiltered magnitude of the SN reported at the time of discovery was ∼16 mag. However, the SN was also visible on *r*-band images taken with the 182 cm Copernico Asiago Telescope on 2015 November 9, 1 week earlier than Nishimura's discovery during routine monitoring of UGC 5460 (Tartaglia et al. 2015). Using the spectrum taken on 2015 November 17.17 UT, it was classified as a Type II SN a couple of weeks after explosion. The spectrum, in fact, showed prominent Balmer lines, Ca H & K, Fe II and also weak He I features (Tartaglia et al. 2015, for a discussion on the explosion epoch, see Section 4). At a redshift of $z = 0.0036$ (de Vaucouleurs et al. 1991), the Virgo infall distance of UGC 5460 is 19.2 ± 1.4 Mpc while the 3K CMB distance is 17.5 ± 1.2 Mpc (from NED where $H_{\rm o} = 73.0 \pm 5$ km s^{-1} Mpc^{-1} and using the flow model of Mould et al. (2000)). NED reports the minimum and the maximum estimated redshift-independent Tully–Fisher distances to be 15.7 Mpc (Bottinelli et al. 1985) and 19.8 Mpc (Tully & Fisher 1988), respectively. The latter is in agreement with the Virgo infall distance (19.2 Mpc), which is the one adopted by Roming et al. (2012), who found for SN 2011ht $M_v = -17$ mag, which is typical of a core-collapse SNe. Consequently, we also adopt the same distance, 19.2 Mpc, for SN 2015as in this paper.

The galactic reddening in the direction of SN 2015as is modest, $E(B-V) = 0.008 \pm 0.001$ mag (Schlafly & Finkbeiner 2011). The low-resolution spectra of SN 2015as (see Section 5) do not show the presence of the narrow interstellar Na I doublet (Na ID) absorption feature at the redshift of UGC 5460, suggesting that the extinction due to host galaxy dust is small. We therefore adopt $E(B-V) = 0.008 \pm 0.001$ mag as the total reddening, corresponding to $A_{\rm V} = 0.025$ mag adopting the reddening law $R_V = 3.1$ (Harris 1973).

[1] http://www.cbat.eps.harvard.edu/unconf/followups/J10081137+5150409.html

3 DATA ACQUISITION AND REDUCTION

3.1 Photometric observations

Photometric follow-up observations of SN 2015as were carried out a few days after the discovery using four ground-based optical telescopes. The observations were performed with the 104 cm Sampurnanand Telescope (ST; Sagar 1999), the 130 cm Devasthal Fast Optical Telescope (DFOT; Sagar et al. 2012) located in ARIES India, the 182 cm Ekar Asiago Copernico Telescope, Italy,[2] and the 200 cm Himalayan Chandra Telescope (HCT; Prabhu & Anupama 2010), Indian Astronomical Observatory (IAO), India. The imaging observations were done using Johnson–Cousins–Bessell *B, V, R, I* and SDSS *u, g, r, i, z* filters. With the 104 cm ST, a 1K × 1K CCD camera was used, with a pixel scale of 0.37 arcsec pixel^{-1}, covering a 6.2 × 6.2 arcmin^2 field of view, while for the 130 cm DFOT, a 512 × 512 CCD was used with a plate scale of 0.63 arcsec pixel^{-1} and covering 5.4 × 5.4 arcmin^2 area in the sky. The Asiago Faint Object Spectrograph and Camera (AFOSC) in Ekar Asiago telescope uses a 2K × 2K CCD with a plate scale of 0.26 arcsec pixel^{-1}. The 4K × 2K CCD on Himalayan Faint Object Spectrograph and Camera (HFOSC) was used for imaging with the HCT. The central 2K × 2K pixels on the chip were used for imaging which covers a 10 × 10 arcmin^2 region on the sky.

Photometric monitoring of SN 2015as started on 2015 November 16 and continued up to 2017 March 28. Along with science frames, several bias and twilight flat frames were also collected. Bias, flat-field and cosmic ray corrected images were obtained and reduced using standard packages in IRAF.[3] Instrumental magnitudes of the SN and field stars were obtained through aperture photometry (using DAOPHOT[4] package), with an optimal aperture which was usually three times the full width at half-maximum (FWHM) of the stellar profile found using an aperture growth curve. PSF photometry was also performed, and using the field stars we obtained a well sampled PSF profile. This modelled PSF profile was used to measure the magnitudes of the SN and field stars. Even though the SN is located in the outskirts of its host galaxy – well isolated from significant contaminating sources – we preferred using the PSF magnitudes which minimizes any possible background contamination.

The Landolt standard fields (Landolt 1992) PG0918, PG0942, PG1323, PG1633, and SA98 were observed with HFOSC in the same nights as the SN field in the *B*, *V*, *R*, and *I* bands. These standard fields allowed us to convert the instrumental magnitudes into apparent magnitudes. Observations were performed under good photometric conditions, with airmass varying between 1.1 and 1.5 and a typical seeing of 1.1 arcsec in the *V* band. Instrumental and catalogue magnitudes of standard field stars were used to obtain zero-points and colour coefficients of the transformation equation, fitted using the least square regression technique, as described in Stetson (1992). The average values of the colour coefficients and zero-points obtained from the least-squares fit of 2016 April 8 and April 12 resulted in the following transformation equations

$$(V - v) = 0.819 - 0.058(B - V) + k_v Q,$$
$$(B - b) = 1.404 + 0.044(B - V) + k_b Q,$$
$$(I - i) = 1.047 - 0.040(V - I) + k_i Q,$$
$$(R - r) = 0.823 - 0.070(V - R) + k_r Q,$$

[2] http://www.oapd.inaf.it/index.php/en/asiago-site/telescopes-and-instrumentations.html
[3] Image Reduction and Analysis Facility.
[4] Dominion Astrophysical Observatory + Photometry.

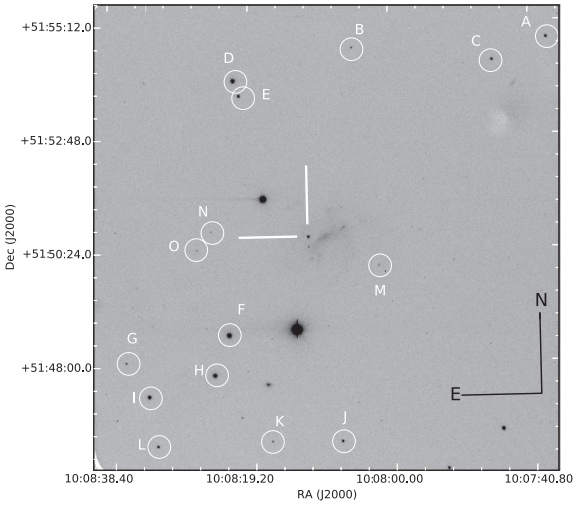

Figure 1. SN 2015as and the local standard stars in the field of UGC 5460. *R*band, 300 s image obtained on 2016 February 24 with the 200 cm HCT.

where Q is the airmass and k_λ are the extinction coefficients. To correct for the atmospheric extinction, we used the site extinction values $k_v = 0.12 \pm 0.04$, $k_b = 0.21 \pm 0.04$, $k_i = 0.05 \pm 0.03$, and $k_r = 0.09 \pm 0.04$ mag airmass^{-1} (Stalin et al. 2008). A root-mean-squared (rms) scatter between transformed and standard magnitude of Landolt stars was found to be between 0.02 and 0.03 mag in the *BVRI* bands. Using these transformation equations, we calibrated 15 non-variable local standards in the SN field. These secondary standards are used to convert the SN instrumental magnitudes into apparent magnitudes in *BVRI* filters from EKAR/AFOSC, ST/1K × 1K CCD and DFOT/512 × 512 CCD. The local secondary standards in the SN field are marked in Fig. 1 , and their magnitudes are listed in Table 1. For each night, precise zero-points were determined using these secondary standards in order to correct for non-photometric conditions. The errors due to calibration and photometry were added in quadrature to estimate the final error in the SN magnitudes. The final SN magnitudes and their associated errors are listed in Table 3.

The SN magnitudes in the *ugriz* bands, obtained with the 182cm Ekar Asiago telescope were differentially calibrated using secondary standards obtained from SDSS DR12 (Eisenstein et al. 2011). We selected seven out of the 15 standard stars that are marked in Fig. 1 with known Sloan *ugriz* magnitudes. They are listed in Table 2, while the Sloan-band SN magnitudes are listed in Table 3.

The *Swift* satellite (Gehrels 2004a,b), equipped with the Ultra-Violet Optical Telescope (UVOT; Roming et al. 2005), began observations of SN 2015as on 2015 November 16, and observed the SN field four times spaced 2 d apart. The *Swift* UVOT data were reduced using the procedure for the *Swift* Optical/Ultraviolet Supernova Archive (SOUSA; Brown et al. 2014). A pre-explosion image from 2012 June was used to subtract the contaminating host galaxy flux. The UVOT magnitudes are given in Table 4.

3.2 Spectroscopic observations

We obtained low- and medium-resolution optical spectra of SN 2015as at 24 epochs (from 2015 November 17 to 2016 June 23), using the 182 cm Ekar Asiago telescope equipped with AFOSC (Grisms Gr 4, VPH 6, and VPH 7) and HCT HFOSC (Grisms Gr 7 and Gr 8) (see Table 5). A combination of grisms was frequently used to cover the entire optical region. The 2D spectra were

Table 1. Star ID and the magnitudes in *BVRI* filters of the 15 secondary standards in the field of SN 2015as.

Star ID	α (h:m:s)	δ ($^\circ$ $'$ $''$)	B (mag)	V (mag)	R (mag)	I (mag)
A	10:07:38.619	+51:54:47.56	17.91 ± 0.02	16.45 ± 0.01	15.24 ± 0.01	14.57 ± 0.01
B	10:08:05.918	+51:54:39.08	19.02 ± 0.02	18.30 ± 0.01	17.61 ± 0.01	17.50 ± 0.02
C	10:07:46.080	+51:54:20.63	17.49 ± 0.02	16.77 ± 0.01	16.07 ± 0.01	15.97 ± 0.01
D	10:08:21.902	+51:54:02.51	15.29 ± 0.02	14.45 ± 0.01	13.68 ± 0.01	13.53 ± 0.01
E	10:08:21.899	+51:54:03.94	17.16 ± 0.02	16.40 ± 0.01	15.68 ± 0.01	15.56 ± 0.01
F	10:08:22.652	+51:48:37.21	14.69 ± 0.02	14.01 ± 0.01	13.33 ± 0.01	13.26 ± 0.01
G	10:08:36.587	+51:48:10.04	18.53 ± 0.02	18.02 ± 0.01	17.40 ± 0.01	17.38 ± 0.02
H	10:08:24.906	+51:47:54.81	15.18 ± 0.02	14.51 ± 0.01	13.84 ± 0.01	13.78 ± 0.01
I	10:08:33.907	+51:47:26.63	15.85 ± 0.02	15.32 ± 0.01	14.70 ± 0.01	14.67 ± 0.01
J	10:08:07.421	+51:46:21.31	17.11 ± 0.02	16.67 ± 0.01	16.10 ± 0.01	16.07 ± 0.01
K	10:08:16.957	+51:46:21.78	19.63 ± 0.03	18.27 ± 0.01	17.13 ± 0.01	16.64 ± 0.01
L	10:08:32.515	+51:46:19.18	17.27 ± 0.01	16.68 ± 0.01	16.03 ± 0.01	15.97 ± 0.01
M	10:08:01.813	+51:50:02.90	20.02 ± 0.05	18.74 ± 0.03	18.17 ± 0.04	17.61 ± 0.02
N	10:08:25.579	+51:50:53.46	20.36 ± 0.06	18.92 ± 0.03	18.07 ± 0.06	17.27 ± 0.04
O	10:08:27.179	+51:50:28.09	19.66 ± 0.05	19.14 ± 0.02	18.82 ± 0.05	18.54 ± 0.06

Table 2. Star ID and the magnitudes in the *ugriz* filters of 7 secondary standards (taken from SDSS DR12) in the field of SN 2015as.

Star ID	α (h:m:s)	δ ($^\circ$ $'$ $''$)	u (mag)	g (mag)	r (mag)	i (mag)	z (mag)
D	10:08:21.902	+51:54:02.51	16.47 ± 0.18	14.82 ± 0.13	14.22 ± 0.13	13.98 ± 0.10	13.88 ± 0.11
E	10:08:21.899	+51:54:03.94	18.28 ± 0.19	16.71 ± 0.15	16.18 ± 0.14	15.98 ± 0.16	15.94 ± 0.13
F	10:08:22.652	+51:48:37.21	15.62 ± 0.11	14.24 ± 0.12	13.81 ± 0.11	13.64 ± 0.15	13.60 ± 0.10
G	10:08:36.587	+51:48:10.04	16.13 ± 0.15	14.75 ± 0.16	14.32 ± 0.10	14.17 ± 0.12	14.16 ± 0.13
M	10:08:01.813	+51:50:02.90	20.81 ± 0.24	18.93 ± 0.20	18.05 ± 0.20	17.68 ± 0.19	17.38 ± 0.15
N	10:08:25.579	+51:50:53.46	20.39 ± 0.22	19.30 ± 0.21	19.01 ± 0.19	18.93 ± 0.20	18.90 ± 0.20
O	10:08:27.179	+51:50:28.09	22.39 ± 0.28	19.71 ± 0.23	18.36 ± 0.18	17.77 ± 0.18	17.48 ± 0.15

pre-processed using standard tasks in IRAF, as for the subsequent extraction and calibration of the 1D spectra. FeNe, FeAr, HgCdNe arc lamps were used for wavelength calibration, whose accuracy was checked using night-sky emission lines. When appropriate, rigid wavelength shifts were applied. The spectroscopic standards GD71, BD+75d325, and Feige34 were observed for correcting the instrumental response and for flux calibration. The flux-calibrated spectra in the blue and the red regions were combined after scaling to get the final spectrum on a relative flux scale. The spectroscopic flux were checked with the photometric measurements at similar epochs and appropriate scaling factors were applied. Finally, the spectra were corrected for redshift.

4 PHOTOMETRIC RESULTS

4.1 Estimation of explosion epoch

The SN was estimated to be 2–3 weeks post-explosion from a preliminary spectroscopic analysis of the spectrum taken on 2015 November 17 (Tartaglia et al. 2015). Although SN 2015as was discovered on 2015 November 15, a pre-discovery r-band detection was obtained on 2015 November 9 during routine monitoring of the galaxy UGC 5460 with the Asiago telescope. From this image, we measured a SN flux corresponding to $r(AB) = 17.59 \pm 0.02$ mag. We applied the SNID (Blondin & Tonry 2011) spectral cross-correlation tool to the spectra of SN 2015as taken on 2015 November 17 and December 03. In order to infer the SN explosion epoch, SNID cross-correlated the spectra of SN 2015as with other Type IIb templates, finding that the explosion occurred around 2015 November 5. The other tool GEneric cLAssification TOol (GELATO) (Harutyunyan et al. 2008), which compares bins of the spectrum with those of template SNe, suggests the explosion occurred around 2015 November 2. Both results agree with the phase reported by Tartaglia et al. (2015). SN 2015as was detected by the Catalina Real Time Transient Survey (CRTS) (Drake et al. 2009) on 2015 November 8. Assuming the CRTS unfiltered magnitudes to be close to V band, we combine our V-band data and CRTS data and perform a parabolic fit. CRTS applies transformations to the observed clear band magnitudes and the converted magnitudes are close to V band. The magnitudes are converted to flux and the fit is performed using the data up to nearly 38 d since discovery. The best-fitting coefficients are used to find the roots of the equation i.e. to the value of time for which the flux equals zero. The best-fitting parabola is shown with the data in Fig. 2(A). From the best-fitting coefficients, the roots obtained are −8.01 and +35 d. The first data point was on 2015 November 8 which is −6.4 d before discovery, so we estimate −8 d i.e. 2015 November 6, as the explosion date.

Drout et al. (2011) estimate that for Type IIb and Ib SNe, explosion dates are usually ∼20 d prior to the V-band maximum. Moreover, SNe IIb exhibit the reddest $(B - V)$ colour ∼40 d after explosion (Pastorello et al. 2008). So, these two findings could serve as further tools to estimate the explosion epoch. We compared the evolution of $(B - V)$ colours of SN 2015as with a few well-studied SNe IIb. We matched the maximum of $(B - V)$ colour of SN 2015as and applied a shift in phase to find the best matching SN from the SN IIb sample. The $(B - V)$ colour evolution matching suggests $(B - V)$ maximum occurred around 14 ± 1 d from discovery, thus the explosion epoch is again around 2015 November 6 (±1) d. This comparison gives an excellent match of SN 2015as with SNe 2008ax and 2010as (see Fig. 2 B) which gives us an explosion epoch around

Table 3. Log of optical observations.

Date	JD	Phase[a] (d)	u (mag)	g (mag)	r (mag)	i (mag)	z (mag)	Telescope
2015/11/09.18	2457335.68	3.17	–	–	17.49 ± 0.01	–	–	EKAR
2015/11/17.18	2457343.68	11.18	16.65 ± 0.01	–	15.37 ± 0.01	15.67 ± 0.01	15.88 ± 0.02	EKAR
2015/12/03.16	2457360.64	28.14	–	–	14.60 ± 0.02	14.67 ± 0.02	–	EKAR
2015/12/10.08	2457366.56	34.06	17.18 ± 0.01	15.42 ± 0.01	14.71 ± 0.01	14.77 ± 0.01	15.01 ± 0.01	EKAR
2015/12/17.21	2457374.69	42.20	18.13 ± 0.02	15.87 ± 0.01	14.97 ± 0.01	14.95 ± 0.01	15.07 ± 0.01	EKAR
2016/01/18.91	2457406.53	74.03	–	16.78 ± 0.01	16.06 ± 0.01	15.88 ± 0.01	15.73 ± 0.01	EKAR
2016/01/19.93	2457407.43	74.93	18.60 ± 0.06	16.77 ± 0.01	16.04 ± 0.01	15.87 ± 0.01	–	EKAR
2016/02/04.05	2457423.52	91.02	18.54 ± 0.04	16.91 ± 0.01	16.29 ± 0.01	16.17 ± 0.01	15.91 ± 0.01	EKAR
2016/02/11.07	2457429.58	97.08	18.75 ± 0.03	16.96 ± 0.01	16.39 ± 0.01	16.29 ± 0.01	16.00 ± 0.01	EKAR
2016/03/17.92	2457465.39	132.89	18.80 ± 0.02	17.42 ± 0.01	16.85 ± 0.01	16.88 ± 0.01	–	EKAR
2016/04/27.90	2457506.42	173.93	–	17.98 ± 0.02	17.35 ± 0.01	17.64 ± 0.01	–	EKAR
2016/05/17.94	2457526.40	193.90	–	18.28 ± 0.03	17.64 ± 0.02	18.07 ± 0.03	17.79 ± 0.02	EKAR
2016/06/23.92	2457563.39	230.89	–	18.42 ± 0.01	18.13 ± 0.01	18.94 ± 0.09	18.58 ± 0.01	EKAR
2016/11/30.09	2457722.58	390.08	–	19.60 ± 0.03	19.79 ± 0.06	20.70 ± 0.01	20.53 ± 0.01	EKAR
2017/03/28.96	2457841.44	508.94	–	–	20.97 ± 0.12	21.68 ± 0.08	–	EKAR

Date	JD	Phase[a] (d)	B (mag)	V (mag)	R (mag)	I (mag)	Telescope
2015/11/17.17	2457343.67	11.16	15.79 ± 0.01	15.52 ± 0.01	–	–	EKAR
2015/12/01.94	2457358.43	25.93	14.92 ± 0.02	14.55 ± 0.04	13.97 ± 0.01	14.26 ± 0.01	DFOT
2015/12/03.16	2457360.64	28.14	15.07 ± 0.01	14.65 ± 0.05	–	–	EKAR
2016/12/05.95	2457362.42	29.91	15.24 ± 0.01	–	14.03 ± 0.01	14.30 ± 0.01	DFOT
2015/12/10.08	2457366.56	34.06	15.77 ± 0.01	14.95 ± 0.01	–	–	EKAR
2015/12/17.24	2457374.69	42.18	16.46 ± 0.01	15.32 ± 0.01	–	–	EKAR
2015/12/20.88	2457377.38	44.87	16.47 ± 0.01	15.54 ± 0.01	14.65 ± 0.01	14.68 ± 0.01	DFOT
2015/12/23.83	2457380.31	47.81	16.78 ± 0.01	15.58 ± 0.01	14.70 ± 0.02	14.70 ± 0.01	HCT
2016/01/01.85	2457389.35	56.85	–	15.87 ± 0.01	15.09 ± 0.01	15.02 ± 0.01	ST
2016/01/02.85	2457390.35	57.85	–	15.90 ± 0.01	15.13 ± 0.01	15.07 ± 0.01	ST
2016/01/03.93	2457391.41	58.91	–	15.92 ± 0.02	–	15.06 ± 0.01	ST
2016/01/05.83	2457393.31	60.81	–	15.96 ± 0.02	15.20 ± 0.01	15.14 ± 0.01	ST
2016/01/12.83	2457400.36	67.85	–	16.11 ± 0.04	–	15.24 ± 0.02	ST
2016/01/13.84	2457401.33	68.83	–	16.11 ± 0.04	15.33 ± 0.01	15.25 ± 0.01	ST
2016/01/15.89	2457403.38	70.87	–	16.15 ± 0.05	15.36 ± 0.01	15.27 ± 0.01	DFOT
2016/01/16.96	2457404.44	71.93	–	16.22 ± 0.02	15.38 ± 0.01	15.24 ± 0.01	DFOT
2016/01/18.05	2457406.52	74.02	17.02 ± 0.02	16.27 ± 0.01	–	–	EKAR
2016/01/19.06	2457407.42	74.91	17.06 ± 0.01	16.26 ± 0.01	–	–	EKAR
2016/01/20.94	2457408.43	75.93	–	16.27 ± 0.04	–	–	ST
2016/01/22.88	2457410.36	77.85	17.09 ± 0.01	16.28 ± 0.01	15.47 ± 0.01	15.49 ± 0.01	HCT
2016/01/25.83	2457413.31	80.81	17.12 ± 0.01	16.32 ± 0.01	15.54 ± 0.02	15.51 ± 0.01	HCT
2016/01/30.80	2457418.27	85.77	–	16.44 ± 0.02	15.63 ± 0.01	15.52 ± 0.01	ST
2016/01/31.78	2457419.28	86.77	17.19 ± 0.02	16.45 ± 0.02	15.65 ± 0.01	15.52 ± 0.01	ST
2016/02/01.81	2457420.29	87.79	–	16.46 ± 0.02	–	15.57 ± 0.01	ST
2016/02/02.75	2457421.22	88.72	–	16.47 ± 0.02	15.70 ± 0.01	15.63 ± 0.01	ST
2016/02/05.05	2457423.52	91.02	17.23 ± 0.01	16.48 ± 0.01	–	–	EKAR
2016/02/10.75	2457429.25	96.75	17.31 ± 0.02	16.54 ± 0.01	15.79 ± 0.01	15.64 ± 0.01	ST, EKAR
2016/02/11.86	2457430.34	97.83	–	–	15.82 ± 0.01	15.70 ± 0.02	ST
2016/02/12.83	2457431.31	98.81	17.34 ± 0.02	16.62 ± 0.03	–	15.70 ± 0.03	DFOT
2016/02/13.88	2457432.36	99.85	17.35 ± 0.02	16.65 ± 0.01	15.86 ± 0.02	15.72 ± 0.01	DFOT
2016/02/14.90	2457433.37	100.87	–	16.68 ± 0.03	15.85 ± 0.01	–	ST
2016/02/24.71	2457443.19	110.68	17.46 ± 0.01	16.73 ± 0.01	15.90 ± 0.01	15.86 ± 0.01	HCT
2016/02/27.75	2457446.25	113.75	–	–	16.01 ± 0.01	15.91 ± 0.01	ST
2016/02/28.84	2457447.30	114.79	17.50 ± 0.01	16.76 ± 0.01	16.03 ± 0.01	15.94 ± 0.01	HCT
2016/03/01.81	2457448.29	115.79	–	–	16.06 ± 0.01	15.95 ± 0.01	ST
2016/03/02.75	2457450.25	117.75	–	–	16.09 ± 0.01	–	ST
2016/03/17.91	2457465.39	132.89	17.74 ± 0.01	17.06 ± 0.01	–	–	EKAR
2016/03/18.83	2457466.31	133.81	–	–	16.32 ± 0.01	16.22 ± 0.01	ST
2016/03/28.76	2457476.24	143.74	–	–	16.46 ± 0.01	16.47 ± 0.02	ST
2016/04/08.66	2457487.14	154.64	–	17.60 ± 0.03	16.55 ± 0.02	16.64 ± 0.03	DFOT
2016/04/12.74	2457491.23	158.73	17.95 ± 0.01	–	–	–	HCT
2016/04/20.75	2457499.22	166.72	18.11 ± 0.02	17.88 ± 0.01	16.63 ± 0.01	16.79 ± 0.02	HCT
2016/04/27.94	2457506.43	173.93	18.29 ± 0.02	17.95 ± 0.01	16.75 ± 0.02	16.89 ± 0.01	HCT, EKAR
2016/05/17.97	2457526.40	193.89	18.58 ± 0.05	18.32 ± 0.02	–	–	EKAR
2016/06/30.68	2457570.18	237.68	–	19.10 ± 0.01	17.34 ± 0.02	–	HCT
2016/11/30.10	2457722.57	390.06	–	21.40 ± 0.01	–	–	EKAR
2016/12/06.18	2457728.68	396.18	–	21.50 ± 0.01	–	–	EKAR

[a] Phase has been calculated since explosion JD = 2457332.5.

Table 4. Log of UV observations.

Phase (JD)	*uvw*2 (mag)	*uvw*1 (mag)	*uvm*2 (mag)	*u* (mag)	*b* (mag)	*v* (mag)
2457342.82	18.21 ± 0.18	17.33 ± 0.13	19.23 ± 0.27	15.75 ± 0.07	15.83 ± 0.06	15.48 ± 0.07
2457344.62	18.41 ± 0.22	17.17 ± 0.13	18.95 ± 0.31	15.73 ± 0.08	15.54 ± 0.06	15.17 ± 0.07
2457346.05	17.94 ± 0.13	16.98 ± 0.09	19.14 ± 0.29	15.30 ± 0.06	15.33 ± 0.05	15.09 ± 0.06
2457348.84	17.78 ± 0.13	16.80 ± 0.09	19.06 ± 0.26	14.87 ± 0.05	15.06 ± 0.05	14.84 ± 0.06

Table 5. Log of spectroscopic observations.

Date (UT)	Phase[a] (d)	Grism	Spectral range (Å)	Resolution	Exposure time (s)	Slit width (arcsec)	Telescope
2015/11/17.17	11.1	Gr04	3360–7740	311	1800	1.26	AFOSC, Ekar
2015/12/03.23	27.9	Gr07, Gr08	3800–6840, 5800–8350	1330, 2190	900	0.77, 1.92	HFOSC, HCT
2015/12/05.82	29.8	Gr07, Gr08	3800–6840, 5800–8350	1330, 2190	900	0.77, 1.92	HFOSC, HCT
2015/12/10.88	34.1	VPH6, VPH7	4500–10 000, 3200–7000	500, 470	1500	1.69, 2.50	AFOSC, Ekar
2015/12/17.82	42.1	VPH6, VPH7	4500–10 000, 3200–7000	500, 470	1200	1.69, 2.50	AFOSC, Ekar
2015/12/20.73	44.9	Gr07, Gr08	3800–6840, 5800–8350	1330, 2190	1800	0.77, 1.92	HFOSC, HCT
2015/12/23.45	47.8	Gr07, Gr08	3800–6840, 5800–8350	1330, 2190	600	0.77, 1.92	HFOSC, HCT
2015/12/27.32	51.8	Gr07, Gr08	3800–6840, 5800–8350	1330, 2190	2400	0.77, 1.92	HFOSC, HCT
2015/01/06.56	61.9	Gr07, Gr08	3800–6840, 5800–8350	1330, 2190	1800	0.77, 1.92	HFOSC, HCT
2016/01/18.21	74.0	VPH6, VPH7	4500–10 000, 3200–7000	500, 470	300	1.69, 2.50	AFOSC, Ekar
2016/01/19.14	74.8	VPH6, VPH7	4500–10 000, 3200–7000	500, 470	1800	1.69, 2.50	AFOSC, Ekar
2016/01/20.05	75.0	Gr07, Gr08	3800–6840, 5800–8350	1330, 2190	300	0.77, 1.92	HFOSC, HCT
2016/01/22.08	77.8	Gr07, Gr08	3800–6840, 5800–8350	1330, 2190	1500	0.77, 1.92	HFOSC, HCT
2016/01/30.81	85.7	Gr07, Gr08	3800–6840, 5800–8350	1330, 2190	2100	0.77, 1.92	HFOSC, HCT
2016/02/04.22	90.7	Gr07, Gr08	3800–6840, 5800–8350	1330, 2190	2100	0.77, 1.92	HFOSC, HCT
2016/02/04.12	90.9	VPH6, VPH7	4500–10 000, 3200–7000	500, 470	1200	1.69, 2.50	AFOSC, Ekar
2016/02/10.19	97.0	VPH6, VPH7	4500–10 000, 3200–7000	500, 470	1500	1.69, 2.50	AFOSC, Ekar
2016/02/20.33	106.7	Gr07, Gr08	3800–6840, 5800–8350	1330, 2190	1800	0.77, 1.92	HFOSC, HCT
2016/02/24.12	110.8	Gr07, Gr08	3800–6840, 5800–8350	1330, 2190	2400	0.77, 1.92	HFOSC, HCT
2016/03/17.09	132.8	VPH6, VPH7	4500–10 000, 3200–7000	500, 470	1800	1.69, 2.50	AFOSC, Ekar
2016/03/31.02	146.7	Gr07, Gr08	3800–6840, 5800–8350	1330, 2190	2100	0.77, 1.92	HFOSC, HCT
2016/04/27.01	173.8	VPH6	4500–10000	500, 470	2400	1.69	AFOSC, Ekar
2016/04/28.08	174.6	Gr07, Gr08	3800–6840, 5800–8350	1330, 2190	1200	0.77, 1.92	HFOSC, HCT
2016/06/23.66	230.8	Gr04	3360–7740	311	2400	1.26	AFOSC, Ekar

[a] Phase has been calculated since explosion JD = 2457332.5.

2015 November 6 (±1). Since the overall *V*-band light curve of SN 2015as is similar to that of SN 2011dh, we matched the light curve of SN 2015as with SNe 2010as and 2011dh by applying appropriate shifts in magnitude and phase (see Fig. 2C). This cross-matching of the light curves suggests *V* max occurred on 15 ± 1 d from discovery, thus the explosion epoch is again around 2015 November 6 (±1) d. Accounting for all the above arguments, we finally estimate the explosion date of SN 2015as as 2015 November 6 (±2) (JD = 2457332.5) and use that date throughout the paper.

4.2 Primary light-curve features

The complete multiband (*BVRIugriz* filters) light curves of SN 2015as from 3 to 509 d after explosion, and the early *Swift* UVOT observations are presented in Fig 3. Several SNe IIb exhibit an early, fast evolving light-curve peak. This early peak is not seen in SN 2015as (in analogy with SN 2008ax) which may be either due to the late discovery of the SN or its effective absence. Our observations started 3.1 d after the explosion. The peak magnitudes and epoch of maximum in each filter was estimated by a cubic spline fit. The errors reported are obtained from the interpolated measurements around the peak. The *B*-band maximum occurred 22.0 ± 0.3 d after the explosion, at an apparent magnitude of 14.74 ± 0.02 mag, while the *V*-band maximum occurred 4.0 d after the *B*-band maximum, at an apparent magnitude of 14.63 ± 0.03. The *r* and *i* bands peaked 2.7 and 5.6 d after the *B*-band maximum, with apparent magnitudes of 14.48 ± 0.01 and 14.68 ± 0.01, respectively. The rise times to the light-curve maxima in each band, their JDs at peak and their peak magnitudes are tabulated in Table 6. The *B*-band maximum light is reached 22 d after the first detection, and there is a gradual delay in reaching the maximum light in the redder pass bands.

The light-curve features of SN 2015as are compared with those of other well-studied SNe IIb (cf. Figs 4 and 5). We construct a sample of 10 SNe IIb [SN 1993J (Richmond et al. 1994, 1996); SN 1996cb (Qiu et al. 1999); SN 2003bg (Mazzali et al. 2009); SN 2008ax (Pastorello et al. 2008; Taubenberger et al. 2011); SN 2010as (Folatelli et al. 2014a); SN 2011hs (Bufano et al. 2014); SN 2011dh (Sahu et al. 2013); SN 2011ei (Milisavljevic et al. 2013); SN 2011fu (Kumar et al. 2013; Morales-Garoffolo et al. 2015), and SN 2013df (Morales-Garoffolo et al. 2014)] from the literature. The parameters of the comparison sample are listed in Table 7.

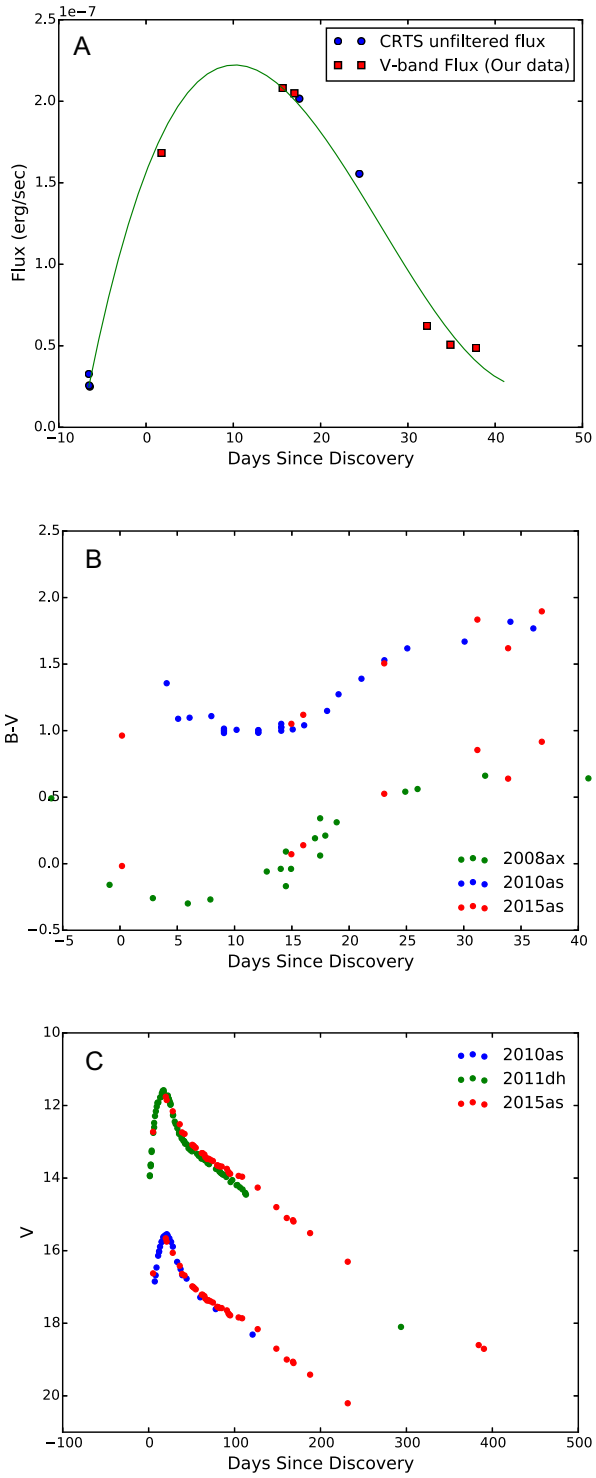

Figure 2. (A) Plot showing parabolic fit of SN 2015as with others along with pre-explosion limit. (B) $B - V$ colour comparison plot of SN 2015as with SNe 2008ax and 2010as. (C) V-band light-curve comparison plot of SN 2015as with SNe 2008ax and 2010as.

SN 2015as shows comparatively larger rise times than other SNe IIb (Table 8). Fig. 4 shows the light-curve evolution of our SN sample up to 100 d. Their observed magnitudes are normalized with respect to their peak magnitudes, and a shift in time is applied to match the time of maximum. At early epochs (pre-max

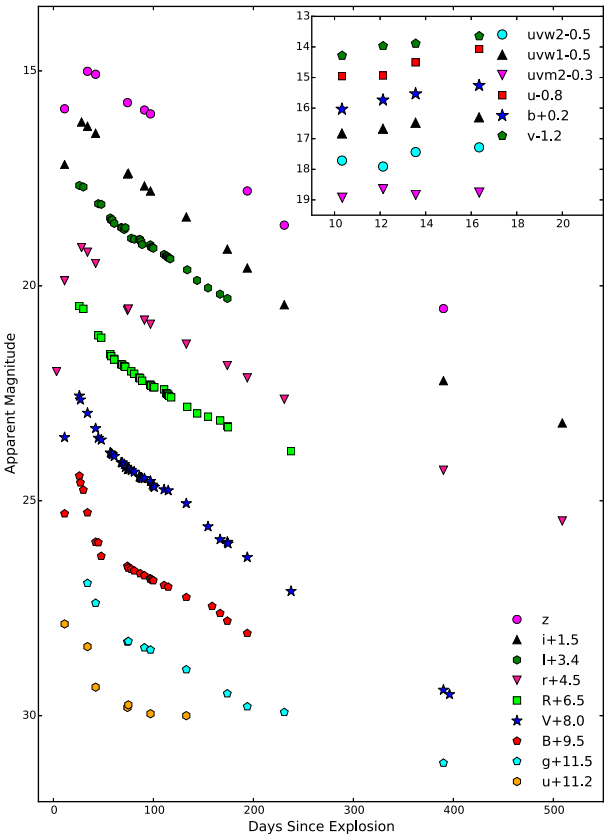

Figure 3. *BVRI*/*ugriz* light-curve evolution of SN 2015as. Inset plot shows the light-curve evolution of the UVOT filters. Explosion epoch is taken as 2015 November 6 (JD = 2457332.5). The light curves are shifted arbitrarily for clarity.

Table 6. Light-curve parameters of SN 2015as.

Band	Peak observed mag (mag)	Peak abs. mag. (mag)	Rise time (d)
B	14.74 ± 0.02	− 16.65 ± 0.39	20.88 ± 0.30
V	14.63 ± 0.03	− 16.82 ± 0.18	24.81 ± 0.79
r	14.48 ± 0.01	− 17.01 ± 0.39	23.53 ± 0.48
i	14.68 ± 0.01	− 16.68 ± 0.38	26.46 ± 0.49

phases), the B and V light curves of SN 2015as clearly resemble those of SNe 2011dh and 1993J. The decline in magnitude during the first 15 d after maximum are $\triangle m_{15}(B) = 1.51 \pm 0.16$ and $\triangle m_{15}(V) = 0.68 \pm 0.03$ mag for the B and V bands, respectively. The V-band decline value is smaller than in other SNe IIb (see Table 7). Our estimate of $\triangle m_{15}(V)$ for SN 2015as is also smaller than the average value for Type Ib/Ic SNe ($\triangle m_{15}(V) = 0.8 \pm 0.1$ mag; Drout et al. 2011). Between 50 and 100 d, SN 2015as declines with rates of 1.10 ± 0.03, 1.85 ± 0.06, 1.87 ± 0.08, and 1.73 ± 0.01 mag $(100\,\mathrm{d})^{-1}$ in the *B, V, R*, and *I* bands, respectively. The decay rate of SN 2015as in B band closely matches that of SN 2011dh whereas it is slower than SN 2011fu. The V-band decline of SN 2015as is faster than SNe 2011dh and 2011fu, whereas the R-band and the I-band decay rates of SN 2015as are slower than SNe 2011dh and 2011fu and are faster than SN 1993J (see Table 9).

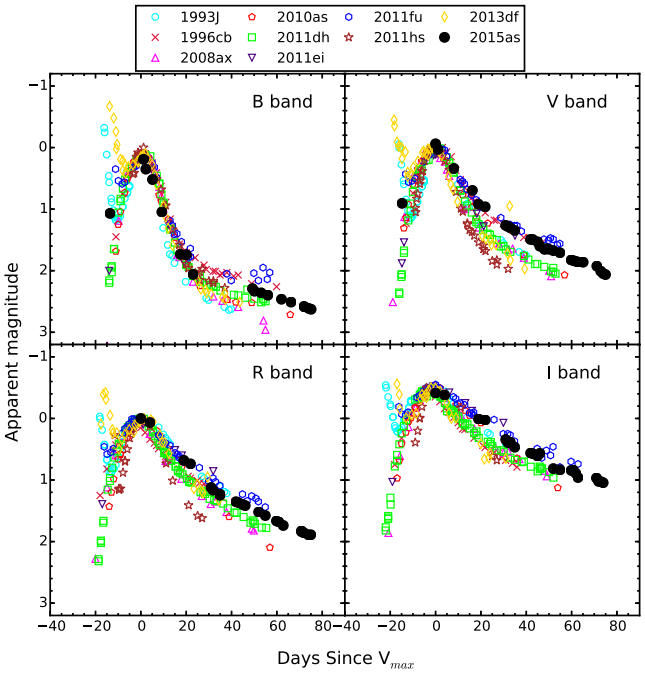

Figure 4. A comparison of light-curve evolution of SN 2015as and other SNe IIb in the different bands up to 100 d post-explosion. The observed magnitudes are normalized with respect to their peak magnitudes and a shift in time is applied to match the epoch of maximum.

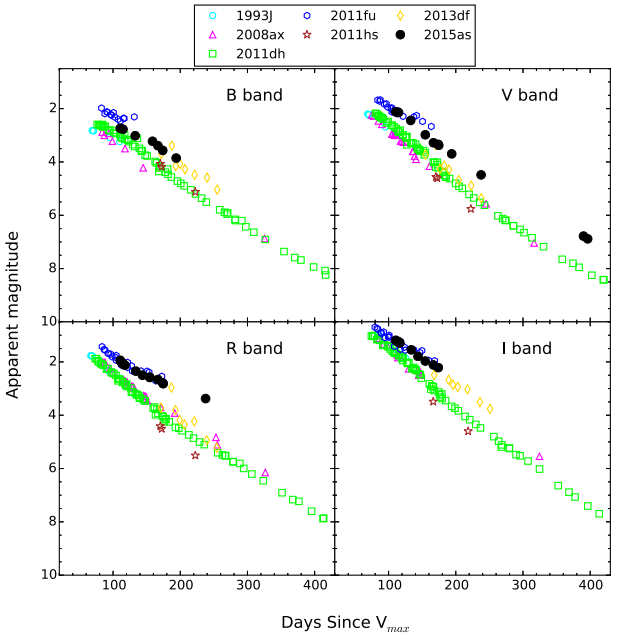

Figure 5. Late-time (80–400 d post-explosion) light-curve evolution of SN 2015as and other SNe IIb. The observed magnitudes are normalized with respect to their peak magnitudes and shifted in time to match the epoch of maximum.

At 100–300 d, the slope of the light-curve changes. A steepening is noticed in the *B* band as compared with other SNe IIb, with the decay rate being 1.30 ± 0.08 mag $(100\,\mathrm{d})^{-1}$, while a softening is noticed in the *V*-band decline with a rate of 1.66 ± 0.04 mag $(100\,\mathrm{d})^{-1}$. The *B*-band steepening may be due to early dust formation. Dust formation always shifts the spectral energy distribution to the redder wavelengths, so early steepening or the fast decay of *B* band could be an indication of early circumstellar interaction leading to dust formation. The *R*- and *I*-band light curves show decay rates of 1.13 ± 0.04 and 1.67 ± 0.03 mag $(100\,\mathrm{d})^{-1}$, respectively. The late-time ($\geq$100 d) evolution of SN 2015as is shown in Fig. 5, along with those of other SNe IIb. The decay rates at comparable epochs for the IIb SN sample are listed in Table 9. The post-maximum light curves of SNe IIb are steeper in the blue bands, with a gradual flattening observed in red bands. The late-time decay rates of SNe IIb usually exceed the $^{56}\mathrm{Co} \rightarrow {}^{56}\mathrm{Fe}$ decay rate (0.98 mag $(100\,\mathrm{d})^{-1}$). This is indicative of incomplete gamma-ray trapping and/or lower positron deposition and is typical in SE SNe. The *B*-band light curve of SN 2015as shows a sort of plateau between 70 and 100 d after explosion, similar to SNe 1993J (Lewis et al. 1994) and 2011fu (Kumar et al. 2013) at comparable epochs.

4.3 Colour curves

The colour evolution of SN 2015as is shown in Fig. 6. SNe 1993J, 2008ax, 2010as, 2011dh, 2011ei, 2011fu, 2011hs, and 2013df are also shown as comparisons. All colour curves have been corrected for the reddening values given in Table 7. The $(B - V)$ colours of SN 2015as become bluer from 11 to 25 d after explosion starting from $(B - V) \sim 0.26$ mag, then becomes redder from about 25 to 50 d after explosion, reaching $(B - V) \sim 1.19$ mag, and evolves towards a blue colour reaching $(B - V) \sim 0.26$ mag at $\sim$190 d. During the first 10–20 d prior to maximum light, the colour of single-peaked SNe IIb like SNe 2008ax, 2010as shows an early red to blue transition that is not detected for double peaked SNe like SNe 1993J, 2011fu, 2013df, etc. (Morales-Garoffolo 2016). SN 2015as shows such early red to blue $(B - V)$ colour transition. The $(V - R)$ moves to redder colours until $\sim$40 d after explosion (reaching 0.86 mag), then becomes bluer from 50 to 90 d. Beyond 170 d, the $(V - R)$ colour grows, and reaches a value of 1.75 mag which is redder than other SNe in the sample. The $(V - I)$ colour becomes redder from 25 to 70 d post-explosion. From 70 to 154 d post-explosion, it remains constant and becomes redder again reaching a value of 1.04 mag at 160 d. At this stage, the outer ejecta becomes optically thin. The redder colour of SN 2015as suggests that the SN is intrinsically redder. We see that NaID due to the Milky Way and the host galaxy are not prominent, hence suggesting very modest extinction.

4.4 Absolute magnitude

The absolute magnitudes of the SN sample are estimated using the distance and reddening values given in Table 7. The distances of all the SNe are calculated assuming $H_0 = 73.0 \pm 5.0$ km s^{-1} Mpc^{-1}. The *V* peak band absolute magnitude of SN 2015as is -16.82 ± 0.18 mag, obtained by adopting the reddening and distance values given in Section 2. The peak absolute magnitude of SN 2015as is nearly 0.5 mag fainter than the mean absolute magnitude (-17.40 ± 0.10 mag; Richardson, Branch & Baron 2006) of SNe IIb and 1.25 mag fainter than average peak absolute magnitude of Type Ib/c SNe. It is fainter than SN 1993J (-17.57 ± 0.24 mag; Richmond et al. 1994), SN 2008ax (-17.61 ± 0.43 mag; Morales-Garoffolo 2016), SN 2010as (-18.01; Morales-Garoffolo 2016), SN 2011dh (-17.12 ± 0.18 mag; Sahu et al. 2013), SN 2011fu (-18.50 ± 0.24 mag; Kumar et al. 2013), while it is nearly 0.5 mag brighter than SN 1996cb (-16.22 mag; Qiu et al. 1999) and SN

Table 7. Properties of the comparison sample.

	SNe	Distance (Mpc)	Extinction $E(B-V)$	M_V (mag)	E_k (10^{51} erg)	$\Delta m_{15}(V)$ (mag)	^{56}Ni mass ($M_\odot$)	M_{ej} ($M_\odot$)	Reference[a]
Type IIb	SN 1993J	3.63 ± 0.7	0.180	−17.59 ± 0.13	0.7–1.4	0.98 ± 0.04	0.10–0.14	1.3–3.5	1, 11
	SN 1996cb	6.41	0.030	−16.22	–	0.97 ± 0.04	–	–	2, 11, 12
	SN 2003bg	21.7	0.024	−16.95	5	0.96 ± 0.03	0.1–0.2	4	3, 11, 12
	SN 2008ax	9.6 ± 1.3	0.422	-17.61 ± 0.43	1–6	0.91 ± 0.03	0.07–0.15	2–5	4, 11
	SN 2010as	27.3 ± 4.7	0.820	−18.01	0.7	0.94 ± 0.05	0.12	2.5	5, 11, 12
	SN 2011dh	8.4 ± 0.7	0.035	−17.12 ± 0.18	0.6–1.0	0.98 ± 0.04	0.05–0.10	1.8–2.5	6, 11
	SN 2011ei	28.5 ± 5.7	0.240	−16.00	2.5	0.75 ± 0.13	0.03	1.6	13
	SN 2011hs	18.3 ± 0.1	0.170	−16.59	0.85	1.18 ± 0.06	0.04	1.8–2.5	7, 11, 12
	SN 2011fu	77.9 ± 5.5	0.218	−18.50 ± 0.24	1.3	0.78 ± 0.04	0.15	3–5	8, 11, 12
	SN 2013df	16.6 ± 0.4	0.090	−16.85 ± 0.08	0.4–1.2	1.32 ± 0.10	0.10–0.13	0.8–1.4	9, 11, 12
Type Ib/Ic				−18.07 ± 0.06					10

[a]*References:* (1) Barbon et al. (1995), Richmond et al. (1994); (2) Qiu et al. (1999); (3) Hamuy et al. (2009), NED; (4) Taubenberger et al. (2011), Pastorello et al. (2008); (5) Folatelli et al. (2014a); (6) Sahu et al. (2013); (7) Milisavljevic et al. (2013); (8) Bufano et al. (2014); (9) Kumar et al. (2013); (10) Morales-Garoffolo et al. (2014); (11) Morales-Garoffolo (2016); (12) Drout et al. (2011); (13) This work.

Table 8. Rise times in *BVri* bands for a sample of Type IIb SNe.

Supernova	Rise time (d)			
	B	*V*	*r*	*i*
SN 1993J	8.8 ± 3.3	8.9 ± 1.4	8.8 ± 1.0	9.1 ± 1.5
SN 2008ax	18.9	20.7	22.3	22.8
SN 2011dh	19.6 ± 0.5	20.6 ± 0.5	21.3 ± 0.5	22.9 ± 0.5
SN 2011fu	13.7 ± 1.4	12.7 ± 1.6	12.9 ± 1.8	13.5 ± 1.8
SN 2015as	20.8 ± 0.3	24.8 ± 0.8	23.5 ± 0.5	26.4 ± 0.5

Table 9. Early- and late-time decay rates of a sample of Type IIb SNe. The sample includes four Type IIb SNe 1993J, 2008ax, 2011dh and 2011fu.

Supernova	*B*	*V*	*R*	*I*	Reference[a]
		Early-time (50–100 d) decay rates in units of mag $(100\,d)^{-1}$			
SN 1993J	1.46	1.73	1.57	1.77	1, 2
SN 1996cb	1.23 ± 0.09	1.96 ± 0.05	2.15 ± 0.06	–	6
SN 2008ax	1.46 ± 0.02	2.05 ± 0.06	2.20 ± 0.07	1.90 ± 0.07	6
SN 2010as	0.80 ± 0.10	1.67 ± 0.04	2.30 ± 0.12	1.96 ± 0.20	6
SN 2011dh	1.09 ± 0.15	1.76 ± 0.04	2.16 ± 0.05	1.90 ± 0.05	2
SN 2011fu	1.25 ± 0.07	1.78 ± 0.04	2.04 ± 0.04	1.97 ± 0.05	5
SN 2013df	1.04 ± 0.04	2.01 ± 0.04	–	–	6
SN 2015as	1.10 ± 0.03	1.85 ± 0.06	1.87 ± 0.08	1.73 ± 0.09	6
		Late-time (100–300 d) decay rates in units of mag $(100\,d)^{-1}$			
SN 1993J	1.39	1.71	1.49	1.87	1, 2
SN 1996cb	–	1.02 ± 0.12	1.17 ± 0.15	–	6
SN 2008ax	1.74 ± 0.30	1.90 ± 0.10	1.64 ± 0.90	2.03 ± 0.80	3, 4
SN 2011dh	1.71 ± 0.13	1.83 ± 0.11	1.51 ± 0.05	1.70 ± 0.06	2
SN 2011hs	1.95 ± 0.12	2.30 ± 0.66	2.03 ± 0.09	–	6
SN 2011fu	–	–	–	–	–
SN 2015as	1.30 ± 0.08	1.65 ± 0.04	1.13 ± 0.04	1.67 ± 0.03	6

[a]*References:* (1) Barbon et al. (1995); (2) Sahu et al. (2013); (3) Pastorello et al. (2008); (4) Taubenberger et al. (2011); (5) Morales-Garoffolo et al. (2015); (6) This work.

2011ei (−16.0 mag; Milisavljevic et al. 2013). SN 2015as is of comparable brightness to SN 2003bg (−16.95 mag; Mazzali et al. 2009), SN 2011hs (−16.59 mag; Bufano et al. 2014), and SN 2013df (−16.85 ± 0.08 mag; Morales-Garoffolo et al. 2014). SNe IIb show a moderate range of *V*-band peak absolute magnitudes (−18 to −16 mag) with SN 2015as belonging to the faint SNe IIb subgroup.

4.5 Bolometric light curve

In order to construct the bolometric light curve, the reddening-corrected magnitudes were converted to fluxes using the flux zero-point values provided by Bessell, Castelli & Plez (1998) and the *u*-band zero-point was taken from Fukugita et al. (1996). The bolometric flux of SN 2015as at different epoch is estimated by integrating the monochromatic fluxes in the *uBVRI* bands using the

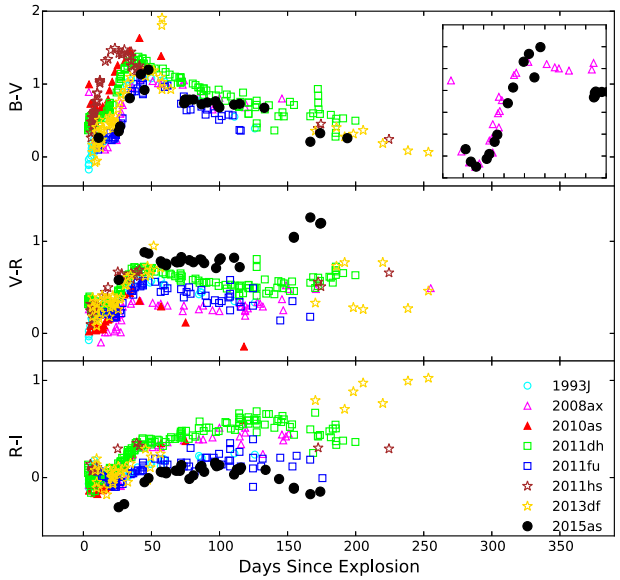

Figure 6. A comparison of the $(B - V)$, $(V - R)$, and $(R - I)$ colours of SN 2015as and other representative SNe IIb. The colours are corrected for the reddening values given in Table 7. The inset in the topmost panel shows the $(B - V)$ colours of SNe 2008ax and 2015as up to ∼80 d post-explosion.

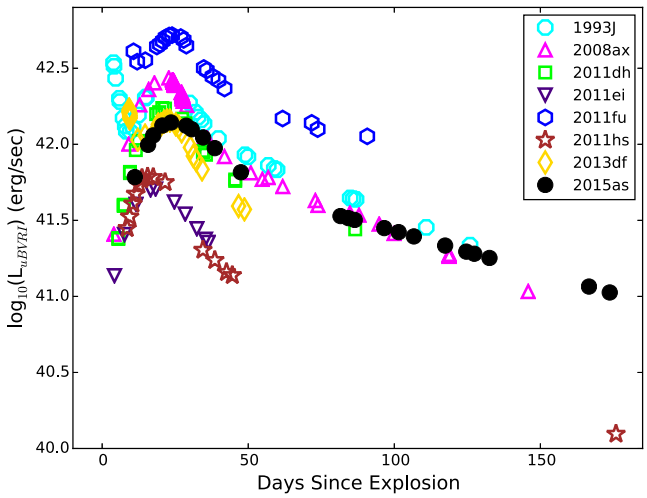

Figure 7. Pseudo-bolometric light curves of our sample of SNe IIb. The distance and reddening values adopted for estimating their bolometric luminosities are given in Table 7.

trapezoidal rule. A distance of 19.2 ± 1.4 Mpc is adopted to convert the flux to bolometric luminosity. Our *u*-band observations end at 132 d after explosion. Assuming a constant $(u - B)$ colour at very late phases, we estimate the *u*-band magnitudes up to 173 d using the constant $(u - B)$ colour equal to the last available one (132 d). We construct the pseudo-bolometric light curve using *uBVRI* observations up to 173 d after explosion. To account for the missing observed flux on some nights, interpolation of the light curves is done. The pseudo-bolometric light curve of SN 2015as is shown along with those of other SNe IIb in Fig. 7. The pseudo-bolometric light curves of SN 1993J (Richmond et al. 1994), SN 2008ax (Pastorello et al. 2008; Taubenberger et al. 2011), SN 2011dh (Sahu et al. 2013), SN 2011ei (Milisavljevic et al. 2013), SN 2011fu (Kumar et al. 2013), SN 2011hs (Bufano et al. 2014), and SN 2013df (Morales-Garoffolo et al. 2014) in the optical domain are constructed with the same method as SN 2015as. The distance and reddening values are given in Table 7. SN 2015as is fainter than most SNe IIb, except SNe 2011hs and 2011ei. In fact, the brightest SN IIb in our sample, SN 2011fu, has a peak luminosity of 5.2×10^{42} erg s^{-1} whereas SN 2015as has a peak luminosity which is a factor 3.2 lower (1.5×10^{42} erg s^{-1}).

Assuming that the radioactive decay of $^{56}\mathrm{Ni} \rightarrow {}^{56}\mathrm{Co} \rightarrow {}^{56}\mathrm{Fe}$ powers the light curve of stripped-envelope SNe, at maximum light the radiated luminosity is directly related to the amount of ^{56}Ni synthesized during the explosion (Arnett 1982). Fixing the peak bolometric peak luminosity (L_p), and assuming the rise time (t_p) being equal to the diffusion time-scale (τ_m), we can estimate the mass of ^{56}Ni using equation 3 of Prentice et al. (2016), which is based on the formulation given by Stritzinger & Leibundgut (2005). Using $L_p(uBVRI) = 1.5 \times 10^{42}$ erg s^{-1}, we estimate the ^{56}Ni mass $= 0.07$ M$_\odot$.

Prentice et al. (2016) also show that the median NIR contribution to the bolometric peak luminosity is 14 per cent and the flux from other wavelengths contribute 10 per cent. The bolometric luminosity increased to 1.7×10^{42} erg s^{-1} when the contribution from NIR and other wavelengths is also considered which results in ^{56}Ni mass of 0.08 M$_\odot$.

Following Arnett (1982), τ_m determines the width of the bolometric light curve and can be expressed in terms of opacity (κ), ejecta mass M_{ej}, and the photospheric velocity at luminosity peak v_{ph}:

$$\tau_m = \sqrt{2}\left(\frac{k}{\beta c}\right)^{\frac{1}{2}}\left(\frac{M_{ej}}{v_{ph}}\right)^{\frac{1}{2}}, \quad (1)$$

where $\beta = 13.8$ is a constant of integration (Arnett 1982) and c is the speed of light. Additionally, we assume a constant opacity $k = 0.07$ cm^2 g^{-1} which is justified if electron scattering is the dominant opacity source (Chevalier 1992). The kinetic energy for spherically symmetric ejecta with uniform density is

$$E_k = \frac{3}{10} M_{ej} v_{ph}^2. \quad (2)$$

In the case of SN 2015as, using $\tau_m = 17$ d and $v_{ph} = 7000$ km s^{-1}, we estimate $M_{ej} = 2.2$ M$_\odot$ and $E_k = 0.656 \times 10^{51}$ erg. Folatelli et al. (2015) use hydrodynamical models to fit the bolometric light curves of SNe 2008ax and 2011dh and generate various model combinations of explosion energy, He core mass and ^{56}Ni mass. A comparison with the models of Bersten et al. (2012) and Folatelli et al. (2015) suggests an He core mass of 3.3 M$_\odot$ in SN 2015as for ^{56}Ni mass $= 0.08$ M$_\odot$ and $E_k = 0.656 \times 10^{51}$ erg. The probable ZAMS mass in this scenario is predicted to be between 12 and 15 M$_\odot$.

The light curves of SNe IIb are usually modelled by a two-component ejecta configuration, with an extended, low-mass, H-rich outer envelope and a denser and compact He-rich core (Nagy et al. 2014; Nagy & Vinkó 2016). The light curve is thus the combination of radiation coming from the shock-heated ejecta and the radioactive decay of ^{56}Ni to ^{56}Co. However, in SNe IIb without the early light-curve peak the ^{56}Ni decay is the dominant source powering the light curve. We assume that SN 2015as is one of these cases. With the assumption that the outer layer retained some H (Arnett & Fu 1989), $\kappa = 0.4$ cm^2 g^{-1} is selected as the Thompson scattering opacity for this layer, while the core is assumed to be composed only by He, and has $\kappa = 0.24$ cm^2 g^{-1}. The model given by Nagy et al. (2014) and Nagy & Vinkó (2016) solves a set of differential equations through simple numerical integration. As the

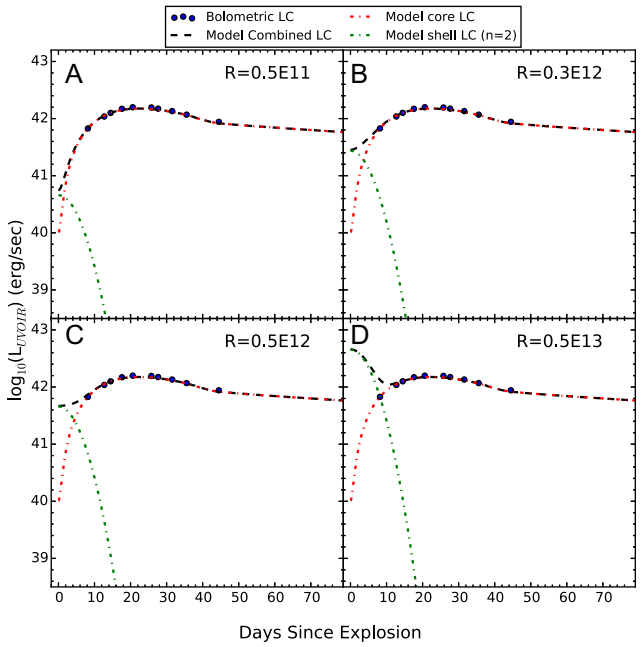

Figure 8. Bolometric light curves at different values of shell radius. The second and third panels show that a small variation in radius incorporates the contribution of the shell to the bolometric light curve.

photon diffusion time-scale is much smaller in the outer shell than in the core, the contribution of the two regions to the overall light curve is well separated. With the two-component model, we are able to extract information on the radius of both the H-rich shell and the He-rich core. Using the *uBVRI* and full bolometric light curves we find the best-fitting model. In order to do so, we vary the shell radius on a wide scale. The contribution of the core and shell at different values of shell radius (while keeping other parameters fixed) is shown in Fig. 8. The transition of the shell radius from 0.3×10^{12} cm to 0.5×10^{12} cm includes the contribution of both the core and the shell to the overall bolometric light curve. Thus, we claim that for a shell radius of 0.5×10^{12} cm a best-fitting model to the full bolometric light curve is obtained (Fig. 8B). The best-fitting values of ^{56}Ni, M_{ej} (core and shell), E_k, E_{Th} (Thermal energy), ionization temperature T and radius of the core and shell, using the *uBVRI* and full bolometric light curve, are given in Table 10. Using the *uBVRI* and full bolometric light curve, our best-fitting model yields ^{56}Ni mass to be 0.07 and 0.08 $M_\odot$, respectively, which are consistent with the estimates obtained using Arnett's formulation as discussed above. However, these parameters are uncertain when the light curve is poorly sampled during its cooling phase. We remark that independent values of opacity, ejected mass and kinetic energy cannot be obtained with this method. Only degenerate combinations like $M_{ej}\kappa$ and $E_k\kappa$ can be constrained by observations. Secondly, for the case of stripped-envelope SNe, the values of M_{ej} and E_k may change significantly when the tail or the peak of the light curves are fitted. The total kinetic energy E_k is the combination of the core and shell.

Comparing with the results obtained with the Arnett's approximation, we found that the estimated values of E_k differ by 0.5×10^{51} erg and M_{ej} is well within comparable range while ^{56}Ni mass also differs by 0.01 $M_\odot$. However, Arnett's formulation works well only when the radius (R) is negligible. For SN 2015as, we estimate a compact radius of 2×10^{11} cm (~3 $R_\odot$) for the He-rich core and 5×10^{11} for the H-rich shell. On the other hand to shock heated ejecta, at the H-recombination front, the thermal energy also contributes in determining the light-curve shape (Arnett 1982; Nagy et al. 2014) or else the assumption that the rise time being equal to diffusion time-scale, would thus lead to a significant underestimate of M_{Ni} and E_k. Also, a minor difference is noticed in the values of M_{ej} as obtained from Arnett's formulation and Nagy & Vinko models, likely due to the discrepant values of κ. Arnett assumes that the electron-scattering opacity is the dominant source of opacity, we therefore vary the opacity between 0.07 and 0.2 cm^2 g^{-1} and estimate M_{ej} being between 1.1 and 2.2 $M_\odot$.

5 SPECTROSCOPIC RESULTS

We present the spectral sequence of SN 2015as from ~11 to ~230 d after the explosion. The first spectrum was taken on 2015 November 17. For the sake of clarity, line identification and spectral evolution at different phases will be discussed in three separate sections.

5.1 Pre-maximum spectroscopic features

Fig. 9 shows the pre-maximum spectrum of SN 2015as, obtained 11 d after the explosion. The spectrum has dominant absorption

Table 10. Best-fitting parameters derived from the analytical modelling of the bolometric light curve using Nagy & Vinkó (2016).

Parameter	Core(He-rich) ($\kappa = 0.24$ cm^2 g^{-1})	Shell(H-rich) ($\kappa = 0.4$ cm^2 g^{-1})	Remarks
Pseudo-bolometric light-curve parameters			
R_0 (cm)	2×10^{11}	0.05×10^{13}	Initial radius of the ejecta
T_{rec} (K)	5500	–	Recombination temperature
M_{ej} ($M_\odot$)	1.0	0.1	Ejecta mass
M_{Ni} ($M_\odot$)	0.08	–	Initial nickel mass
E_{Th}	0.36×10^{51}	0.30×10^{51}	Initial thermal energy
E_{kin}	0.75×10^{51}	0.25×10^{51}	Initial kinetic energy
Full-bolometric light-curve parameters			
	(κ =0.24 cm^2 g^{-1})	(κ =0.4 cm^2 g^{-1})	
R_0 (cm)	2×10^{11}	0.05×10^{13}	Initial radius of the ejecta
T_{rec} (K)	5500	–	Recombination temperature
M_{ej} ($M_\odot$)	1.2	0.1	Ejecta mass
M_{Ni} ($M_\odot$)	0.08	–	Initial nickel mass
E_{Th}	0.36×10^{51}	0.30×10^{51}	Initial thermal energy
E_{kin}	0.78×10^{51}	0.28×10^{51}	Initial kinetic energy

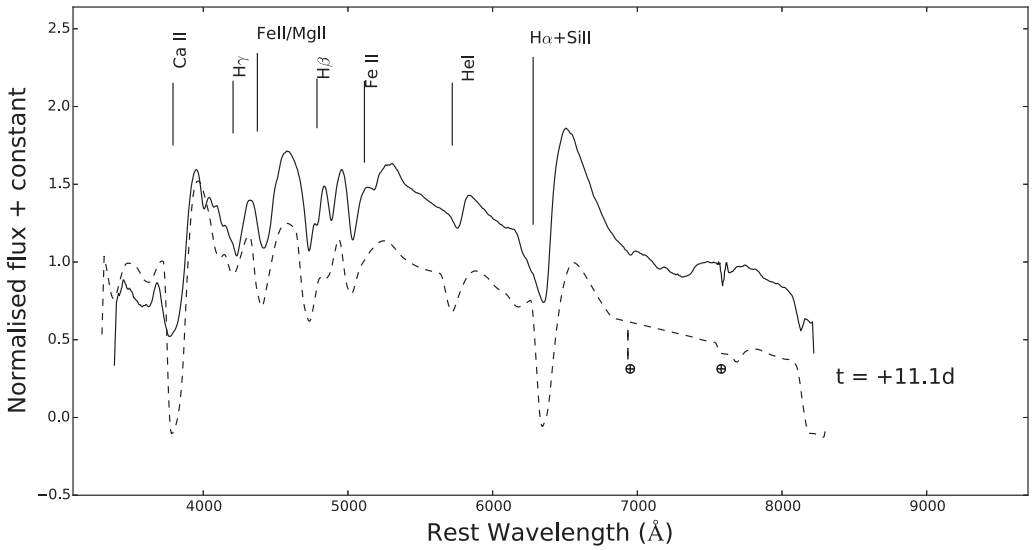

Figure 9. Early spectrum of SN 2015as (11 d after the explosion). The synthetic spectrum generated using SYN++ modelling is plotted with a dashed line.

features superimposed on the continuum. The spectrum is dominated by features of Ca II H & K (3968 and 3933 Å), P Cygni absorption profiles of H α (6563 Å), H β (4861 Å), H γ (4341 Å), and Fe II (4924 and 5018 Å)/Mg II lines. The dip at 4882 Å is most likely due to the combination of He I (4921, 5051 Å) and Fe II (4924 Å) features. We also identify a weak Fe II absorption line at 5038 Å. The feature seen at 5760 Å is very likely due to He I 5876 Å.

The observed spectrum is compared with a synthetic spectrum generated using SYN++ in Fig. 9. SYN++ is an improved version of the SYNOW code (Thomas, Nugent & Meza 2011). The basic assumptions of this model are spherical symmetry, local thermodynamic equilibrium for level populations, resonant scattering line formation above a sharp photosphere and homologous expansion of the ejecta ($v \propto r$). The line formation is treated using the Sobolev approximation (Sobolev 1957; Jeffery 1990). The optical depth of the strongest line is the free fitting parameter, while the optical depths of other lines of the same ion are determined assuming Boltzmann equilibrium at the excitation temperature T_{exc}. However, one should account for approximations due to assuming a sharp photosphere emitting like a blackbody, and no electron scattering.

The main species required to match the observed spectrum are marked in Fig. 9. The photospheric temperature of the synthetic spectrum at 11 d is 8000 K. The photospheric velocity obtained from the synthetic spectrum is $v_{ph} = 8500\,\mathrm{km\ s^{-1}}$. The H lines are detached from the photosphere by a modest amount and with a minimum velocity of $v_{min} = 8800\,\mathrm{km\ s^{-1}}$. The H β and H γ features are reproduced well with a minimum velocity $v_{min} = 8800$ km s^{-1} and maximum velocity $v_{max} = 15\,000\,\mathrm{km\ s^{-1}}$. The broad H α feature is difficult to fit due to the possible blend with a nearby component. Barbon et al. (1995) suggest that the broadness of H α in SN 1993J could be due to a blend of H α and Fe II lines whereas in SN 2000H it could be a blend with C II 6580 Å and Si II 6355 Å line (Elmhamdi et al. 2006; Mazzali et al. 2009; Silverman et al. 2009). Two components of H with different velocities reproduce the broad H α profile in SN 2011ei (Milisavljevic et al. 2013). However, in SN 2015as spectral modelling shows that a two-component H α profile (one being a high-velocity component) does not fit well. On the other hand, a combination of H α and Si II 6355 Å reproduces the observed features at 6353 Å (see Fig. 9). The feature at 5760 Å is due to He I, as also observed in SN 2008ax (Pastorello et al. 2008).

A comparison of the early spectrum of SN 2015as with other SNe IIb is shown in Fig. 10. The sample includes SNe 1993J (Matheson et al. 2000a; Barbon et al. 1995), 1996cb (Modjaz et al. 2014), 2003bg (Hamuy et al. 2009), 2008ax (Taubenberger et al. 2011; Crockett et al. 2008; Modjaz et al. 2014), 2011fu (Morales-Garoffolo et al. 2015; Kumar et al. 2013), 2011dh (Sahu et al. 2013), 2011ei (Milisavljevic et al. 2013), 2011hs (Bufano et al. 2014) and 2013df (Morales-Garoffolo et al. 2014). The H α absorption feature is very prominent in all spectra though with different shapes. It is important to note that the He I 5876 Å feature is very weak in SN 2015as as compared to other members of our sample.

5.2 Transition phase

The second spectrum was obtained 27 d after the explosion, and is shown along with the 29 and 34 d spectra in Fig. 11. The most prominent lines, including the He features, are marked in the figure. A common property of the three spectra is the weakening of the blue continuum. We also note a decrease in the strength of H β and H γ while He I features now become prominent. In particular, P Cygni features due to He I lines 4471, 5015, 5876, 6678, 7065, and 7281 Å are now strong. The appearance and the strengthening of He I 6678 and 7065 Å about a month after the explosion, indicates that the progenitor of SN 2015as was partially stripped. The Fe II lines between 4300 and 5000 Å become stronger with time. A double notch in absorption is seen at 5300 Å probably due to Sc II lines. We also see a O I 8448 Å line near the left edge of Ca II NIR triplet. The O I line later on blends with the increasing Ca II NIR. The H α absorption line becomes somewhat narrower, and a double trough is seen in 27 and 29 d spectra. The red component is primarily due to the P Cygni profile of H α line while the origin of the blue component is still not clear. It has been suggested that the blue component is also a part of H α line, e.g. due to the presence of non-spherical density distribution of H (Schmidt et al. 1993) or the existence of a second high-velocity H α layer (Zhang et al. 1995; Branch et al. 2002). The spectral modelling reveals again that a combination of H α and Si II 6355 Å reproduces the observed features at 6353 Å.

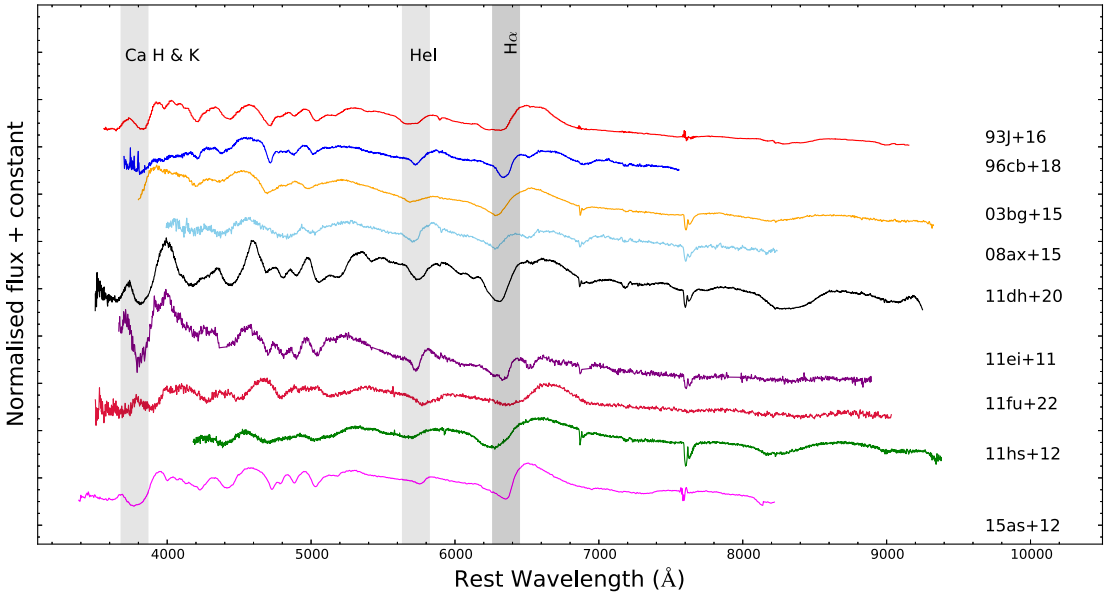

Figure 10. A comparison of the pre-maximum spectrum of SN 2015as with those of SNe 1993J, 1996cb, 2003bg, 2008ax, 2011dh, 2011ei, 2011fu, and 2013df. Even though He I lines are visible, all spectra show strong H α features.

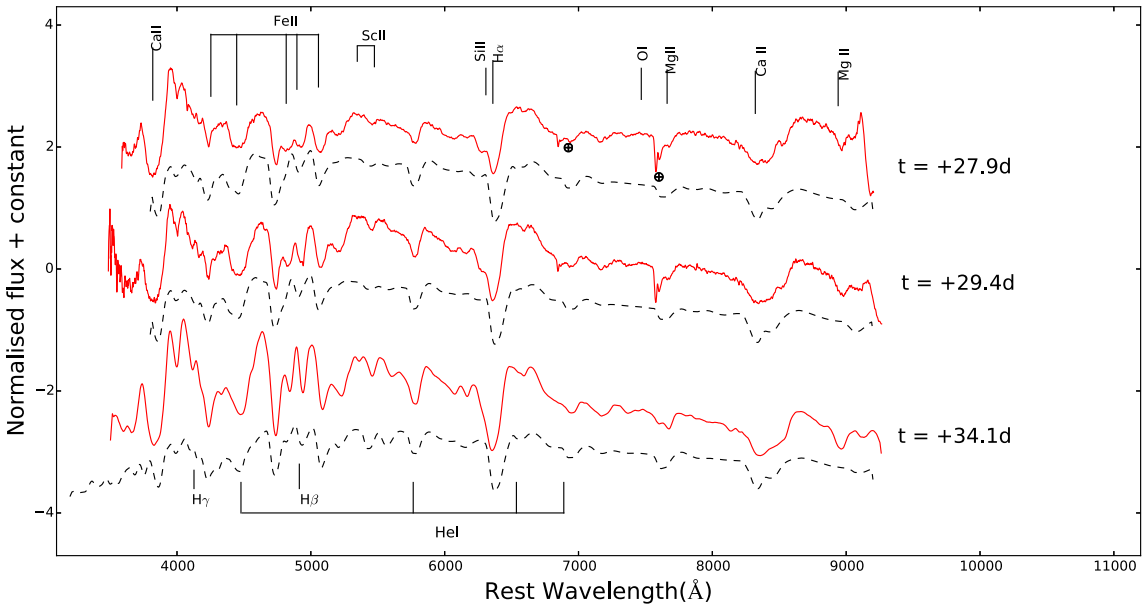

Figure 11. The 27, 29, and 34 d spectra of SN 2015as are characterized by the appearance of He I features. Phases are calculated from the explosion date. All the spectra show strong H α feature and He I feature with varying strength. The synthetic spectra generated using SYN++ are marked with dashed lines. Spectra are vertically shifted by an arbitrary amount for clarity.

A close look at the 27, 29, and 34 d spectra reveals that the H profile becomes sharper. The synthetic spectra using SYN++ with v_{max} decreasing from 12 000 km s^{-1} to 7000 km s^{-1}, and the photospheric temperatures fading from 8000 to 6000 K fit the observed spectra well. The He I 5876 Å feature is well fitted, and the blueshift of its absorption profile indicates velocities decreasing from 8000 to 7000 km s^{-1}. The O I, Ca II, and Mg II lines become prominent, with velocities 7500, 9000, and 8000 km s^{-1}, respectively.

Subsequent spectra, in the transition from the photospheric to the nebular phase, show a weakening of the Ca II H & K feature (see Fig. 12). The absorption of H α decreases in strength with time and, at ∼75 d, it marks the metamorphosis of the SN spectrum from Type II to Type Ib. Lines of He I 4471, 5015, 5876, 6678, 7065, and 7281 Å are now well observed. The presence of H α and H β absorption features until ∼75 d indicates that the progenitor was still relatively H-rich at the time of the explosion. A residual H α emission feature is seen between 75 and 110 d post-explosion. The O I line at 7774 Å is detected, in addition to the absorption due to Mg II. The He I 5876 Å wing is becoming prominent and the He I absorption profile shows a notch due to the Na ID feature. This phase is characterized by the appearance of the Ca II NIR emission feature, which gradually becomes more prominent from the 50 to 110 d spectra. The spectra now resemble those of a Type Ib event, except for the residual presence of the H α feature. The forbidden line of [O I] 5577 Å and O I at 7774 Å become more prominent with time. Fig. 13 shows that the spectrum of SN 2015as at this

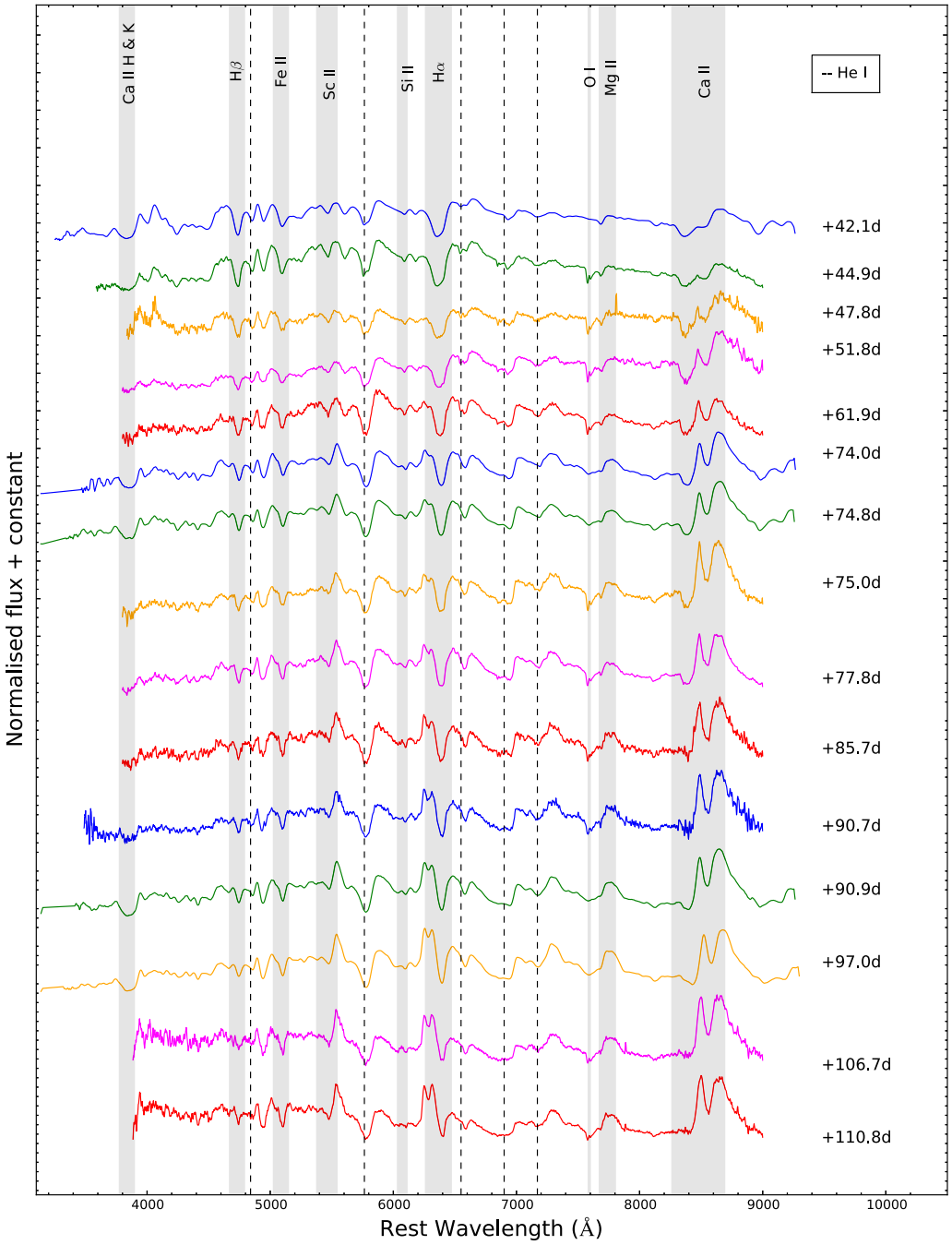

Figure 12. Spectral evolution of SN 2015as from 42 to 110 d after explosion. The important lines are marked by shaded regions. Dotted lines represents the prominent He I features at different stages of the SN evolution.

phase match well those of SNe 1993J, 2008ax and 2011dh. The H α profile at this stage is similar to SNe 2003bg and 1996cb, suggesting a similar progenitor configuration. The Ca II NIR emission of SN 2015as matches those observed in the spectra of SNe 1993J and 2008ax, although the peaks are more pronounced in SN 2015as.

5.3 Nebular phase

The nebular phase spectral evolution from 132 to 230 d after explosion is shown in the Fig. 14. The nebular spectra are dominated by the strong [O I] doublet at 6300, 6364 Å. The 230 d spectrum also shows a prominent [Mg I] 4571 Å line, which has a similar origin as the [O I] doublet. A broad emission likely due to O I 7774 Å is also seen up to 230 d after explosion. The nebular phase spectra of SNe IIb are compared in Fig. 15. We note that H α has faded in all SN spectra which are dominated by emission lines of [Mg I] 4571 Å, [O I] 6300, 6364 Å, [Ca II] 7291, 7324 Å, O I 7774 Å, blends of [Fe II] lines near ∼5000 Å, and the Ca II NIR triplet. The weakening of [O I] 5577 Å line can be noticed. Although nebular features are similar for all SNe, differences exist with respect to the relative strengths of emission lines, and their shapes. The Ca II NIR triplet in SN 2015as is very similar to that of SN 1993J, although the overall spectrum closely matches those of SNe 2008ax and 2011dh. The Ca II NIR feature in SN 2015as has a different emission geometry when compared with SN 2003bg and SN 2011dh (Fig. 15). Although the He I

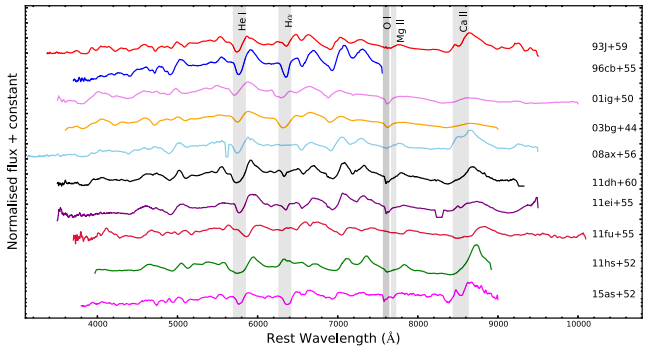

Figure 13. A comparison of SN 2015as and other SNe IIb at intermediate epochs (∼45–60 d) of their evolutions. The spectra show weakening of H lines along with dominant Ca II NIR and He I features. The important lines are marked by shaded regions.

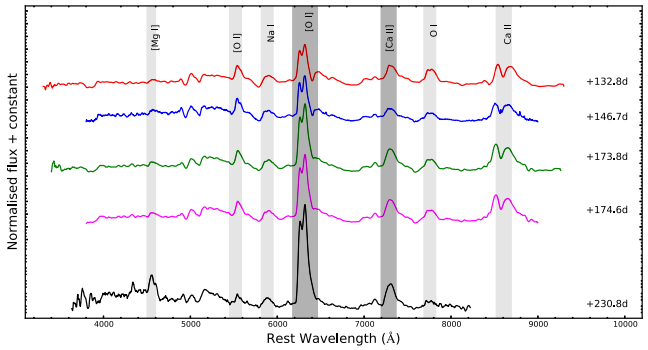

Figure 14. Nebular phase spectral evolution of SN 2015as from 132 to 230 d post-explosion. Prominent lines such as the [O I] and [Ca II] doublets, along with [Mg I] singlet, are marked by shaded regions.

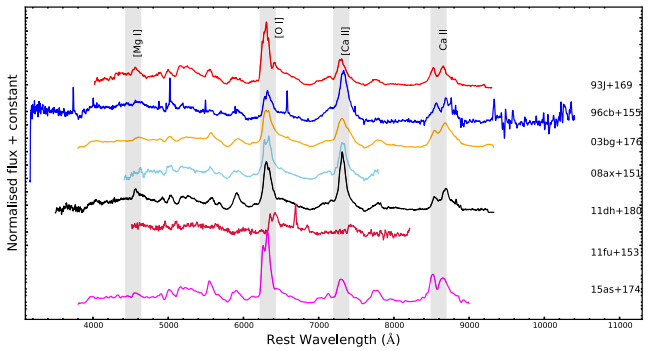

Figure 15. Comparison of the nebular phase spectrum of SN 2015as with other SNe IIb. Prominent doublet of [O I] is marked.

lines at 6678, 7065 Å are now relatively weaker, the He I 5876 Å is still pronounced in SN 2015as and SN 2011dh, most likely due to an increasing contribution of Na ID. We also estimate the [Mg I]/[O I] flux ratio on the last spectrum of SN 2015as, and found the value to be 0.23. Sahu et al. (2013) found that at ∼280 d post-explosion, the ratio is ∼0.2 in SN 2011dh, ∼0.15 in SN 1993J and 0.36 in SN 2001ig, which has the strongest [Mg I] line (Silverman et al. 2009). The emission features of [O I] 6300, 6363 Å, [Ca II] 7291, 7324 Å doublets and [Mg I] 4571 Å singlet are discussed in more detail below.

The Hα absorption is detected up to 146 d in SN 2015as, and completely disappears thereafter. We notice that Hα is seen in the nebular phases (beyond 150 d) in SN 1993J, which is plausibly a signature of circumstellar interaction (Matheson et al. 2000b; Maurer et al. 2010), or due to mixing and clumping of H and He ionized by the radioactive decay (Maurer et al. 2010) or even blending of Hα and [N II] 6548, 6584 Å. In the case of SN 2015as, no nebular Hα emission is observed after 150 d, implying that circumstellar interaction is not significant.

Magnesium emission at late phases: Maeda et al. (2006a), through their hydrodynamic explosion models, suggest that [Mg I] and [O I] have similar spatial evolution within the SN ejecta. A direct comparison of the [Mg I] and [O I] 6300, 6364 Å profiles is problematic as the [O I] feature is a doublet. However, we compare the evolution of the [O I] 5557 Å with [Mg I] 4571 Å. in the case of SN 2015as, the [Mg I] feature is not as prominent as [O I] in the early nebular spectra. This may be due to different geometry originating in the stratification of progenitor star and the hydrodynamics of the explosion. The [Mg I] 4571 Å feature at day 230 shows an asymmetric profile similar to that of [O I]. In Fig. 16(A), we present the evolution of [O I] 5577 Å line profile and compare it with that of [Mg I] at 230 d. The two lines have very similar profiles in the late nebular phase. This indicates that the line profiles are governed by the ejecta geometry, and [O I] and [Mg I] have a similar distribution in the SN ejecta.

Oxygen emission at late phases: The [O I] 6300, 6364 Å usually have a double-peaked structure. Fig. 16(B) shows the evolution of the double peaked [O I] line from 132 to 230 d after explosion. The [O I] line is becoming prominent and more symmetric with time. The wavelength corresponding to zero velocity is that of the 6300 Å line. The two peaks of the [O I] feature in the SN 2015as spectra are separated by 62 Å, and this matches the expectation for the two lines of the [O I] doublet. The absence of [O I] 5577 Å marks the onset of optically thin regime (Taubenberger et al. 2009), predicted with an intensity ratio for the two lines of the doublet of 3:1 (Mazzali et al. 2001; Taubenberger et al. 2009). The observed profile gives information on the geometry of the emitting region (Taubenberger et al. 2009, 2013). In the case of SN 2015as, the ratio of [O I] 6300, 6364 Å to [O I] 5577 Å line fluxes is about 7, hence, the contribution of [O I] 5577Å flux is actually negligible. SN 2015as has one peak close to the rest velocity while the other one is blueshifted by ~ -1700 km s^{-1}. The possible explanations for the observed blueshift are low mode convective instabilities (Scheck et al. 2004; Kifonidis et al. 2006) or the suppression of the redshifted part of the emission spectrum caused by dust formation as the ejecta cool (Matheson et al. 2000b; Elmhamdi et al. 2004). A straightforward geometric explanation could be either asymmetric explosions with the emitting oxygen located in a torus or in a disc perpendicular to the line of sight (Mazzali et al. 2001; Maeda, Mazzali & Nomoto 2006b), or a blob of oxygen moving perpendicularly to the line of sight. For different SNe, multiple explanations were proposed for the origin of double peaked profiles. The [O I] line profile, in most cases is the result of clumpy ejecta with a sawtooth profile (Matheson et al. 2000b), which is supported by the explosion scenario of SN 1987A (Li, McCray & Sunyaev 1993) where the O emission originates from clumps of newly synthesized material, while the Ca emission mainly originated from pre-existing, uniformly distributed material. Filippenko & Sargent (1989) suggested that these enhancements come from Rayleigh–Taylor fingers of high-speed material or changes in local density contrasts. Asphericity in the explosion would also result in asymmetric peaks (Milisavljevic et al. 2010). An alternative explanation for the double peaked structure of O lines could be a high-velocity (12 000 km s^{-1}) Hα absorption component, which causes a split in the [O I] peak

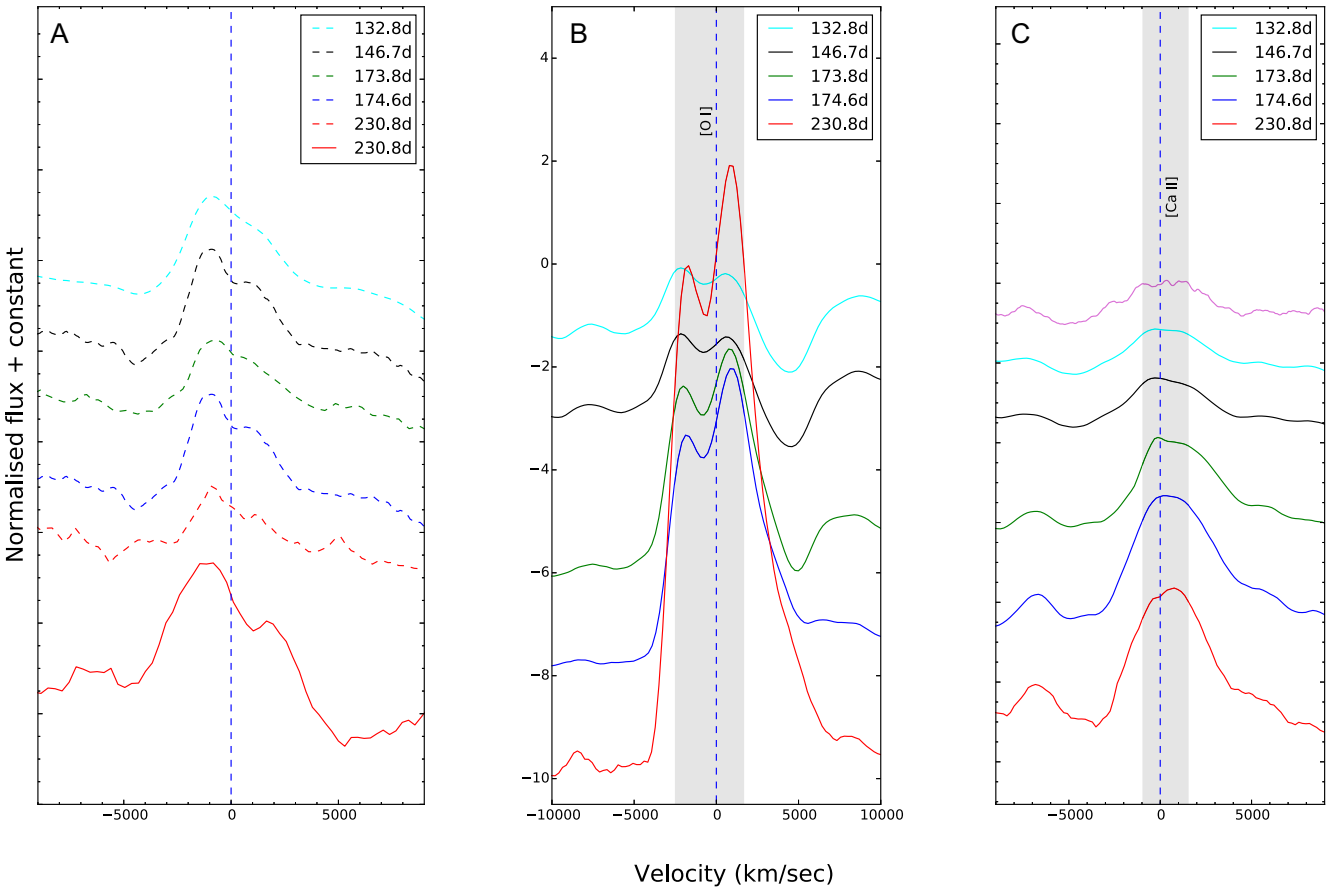

Figure 16. Line profiles of [Mg I] 4571 Å/[O I] 5577 Å, [O I] 6300, 6364 Å, and [Ca II] 7291, 7324 Å during the nebular phase. The first five dashed lines in panel (A) represent the evolution of the [O I] 5577 Å line, while the last one (solid red line) is for [Mg I] 4571 Å.

(Maurer et al. 2010). Since there is no late-time Hα emission in SN 2015as, the contribution of H to the [O I] split can be ruled out. The asymmetric profile of SN 2015as is very similar to that observed for SN 2008ax, that was attributed to a thin O torus viewed from equatorial direction in addition to a spherically symmetric mass of O, or an aspheric distribution of ^{56}Ni exciting the O layers (Taubenberger et al. 2009).

Calcium emission at late phases: As shown in Fig. 15, the [Ca II] 7291, 7324 Å emission in SN 2015as matches that of SN 1993J. The [Ca II] emission line in SN 2015as has a round peak unlike SN 2008ax and SN 2011dh which exhibit sharp peak. Fig. 16(C) shows the [Ca II] evolution from 132 to 230 d after the explosion, with the feature increasing in strength with time. The pre-existing envelope excites the Ca mixed in the atmosphere to reach the temperature required to produce the [Ca II] emission, as H and He do not radiate efficiently (Li et al. 1993; Matheson et al. 2000a). Calcium clumps are formed during explosion but they do not contribute significantly to the [Ca II] emission. They intercept γ-ray radiation, however, as the mass fraction is comparatively less, the amount of radioactive luminosity and temperature achieved is not sufficient for the emission.

5.4 Estimates of the O mass and [Ca II]/[O I] ratio

The line strengths in the nebular phase spectra provide key information on the progenitor mass. Uomoto (1986) derived a relation, showing the minimum mass of O that can be estimated in the high-density ($N_e \geq 10^6$ cm^{-3}) limit. This is given by

$$M_{\rm O} = 10^8 \times D^2 \times F([{\rm O\,I}]) \times \exp^{(2.28/T_4)}, \quad (3)$$

where $M_{\rm O}$ is the mass of the neutral O in M$_\odot$ units, D is distance to the galaxy in Mpc, $F([{\rm O\,I}])$ is the total flux of the [O I] 6300,6364 Å feature in erg s^{-1} cm^{-2}, and T_4 is the temperature of the O-emitting region in units of 10^4 K. Ideally, the ratio of [O I] 5577 Å to the [O I] 6300, 6364 Å feature should be considered. However, the [O I] 5577 Å line is very faint, and the limit of the flux ratio can be assumed to be $\leq$0.1. In this limit two conditions exist, either high density ($N_e \geq 10^6$ cm^{-3}) and low temperature ($T_4 \leq 0.4$ K), and low density ($N_e \leq 10^6$ cm^{-3}) and high temperature ($T_4 = 1.0$ K) (Maeda et al. 2007). The O-emitting region is found at high density and low temperature (Schlegel & Kirshner 1989; Leibundgut et al. 1991; Elmhamdi et al. 2004). Using the observed flux of 4.1×10^{-14} erg s^{-1} cm^{-2} of the [O I] 6300, 6364 Å doublet from the 2016 April 27 spectrum, and adopting $T_4 = 0.4$ K, we estimate $M_{\rm O} = 0.45$ M$_\odot$. The [O I] 7774 Å line is also seen in the nebular spectrum, which is mainly due to the recombination of ionized O (Begelman & Sarazin 1986). This also indicates the presence of O in ionized form, thus $M_{\rm O} = 0.45$ M$_\odot$ can be considered as the lower limit of the O mass ejected during explosion. For the sample of stripped-envelope SNe considered by Elmhamdi et al. (2004), the O mass usually ranges from about 0.2 to 1.4 M$_\odot$. The estimated O mass is 0.5 M$_\odot$ for SN 1993J (Houck & Fransson

1996), 0.1–0.3 $M_\odot$ for SN 1996N (Sollerman, Leibundgut & Spyromilio 1998), 0.2 $M_\odot$ for SN 2007Y (Stritzinger et al. 2009), 1.3 $M_\odot$ for SN 2003bg (Mazzali et al. 2009), and 0.22 $M_\odot$ for SN 2011dh (Sahu et al. 2013). The O mass for SN 2015as is hence similar to that of SN 1993J.

The O layer formed during the hydrostatic burning phase is responsible for the [O I] emission. The ejected mass of O is directly related to the main-sequence progenitor mass. Thielemann, Nomoto & Hashimoto (1996) made explosive nucleosynthesis calculations and predicted major nucleosynthesis yields for the progenitor mass of 13–25 $M_\odot$. For progenitor masses of 13, 15, 20, and 25 $M_\odot$, Thielemann et al. (1996) showed that the corresponding O masses would be 0.22, 0.43, 1.48, and 3.0 $M_\odot$, respectively. Thielemann et al. (1996) also estimated He core masses of 3.3, 4, and 8 $M_\odot$, corresponding to progenitors of 13, 15, and 25 $M_\odot$, respectively. Adopting the O mass estimate for SN 2015as to be 0.45 $M_\odot$, the corresponding progenitor mass would be a ∼15 $M_\odot$ with a He core mass ∼4 $M_\odot$. The ratio of the [Ca II] 7291–7324/[O I] 6300–6364 fluxes serves as an indicator for estimating the main-sequence mass of the progenitor. The O mass primarily depends on the mass of the progenitor, while Ca is mostly independent of it, so a small ratio of this flux would point to a high progenitor mass (Nomoto et al. 2006). Indeed, Fransson & Chevalier (1989) have shown that the variations in the composition of the He core mass lead to substantial differences in the spectra, especially in the [Ca II]/[O I] emission-line ratio. The He core masses and thus the progenitor mass can be estimated from such [Ca II]/[O I] ratio. For SN 2015as, the ratio of [Ca II]/[O I] at 174–230 d is found to be nearly constant, around 0.44. The value is lower than that measured for SN 1993J (∼0.5) with progenitor mass 14–16 $M_\odot$, SN 1996cb (∼2), SN 2003bg (∼0.5) with progenitor mass 22–25 $M_\odot$, SN 2008ax (∼0.9) with progenitor mass 18.6 $M_\odot$, SN 2011hs (∼1.2) with progenitor mass 11–15 $M_\odot$ and SN 2011dh (∼0.8) with progenitor mass 13–18 $M_\odot$ at comparable epochs (Deng et al. 2001; Mazzali et al. 2009; Chornock et al. 2011; Taubenberger et al. 2011; Sahu et al. 2013; Bufano et al. 2014). Kuncarayakti et al. (2015) compared this ratio for a group of stripped-envelope SNe, and found that it is not sensitive to density and temperature changes, while depends extensively on the progenitor mass. They also found that this ratio remains nearly constant during the nebular phases, and never exceeds the value of ∼0.7 for Type II SNe, while a considerable diversity exists for Type Ib/Ic events (Fransson & Chevalier 1989; Jerkstrand 2017). The estimated value is similar to that measured for SN 1993J and SN 2003bg. The low flux ratio is indicative of a lower abundance of [Ca II] in the pre-existing envelope. Moreover, the [Ca II] doublet sometime gets blended with [O II] (as in SN 1995N; see Fransson et al. 2002) and for such cases the ratio of [Ca II]/[O I] may not be a good proxy for core mass estimation. The probable progenitor scenario for SN 2015as is either a 14–15 $M_\odot$ star in a binary association like in the case of SN 1993J or a Wolf–Rayet star of 20–25 $M_\odot$ mass like SN 2003bg.

5.5 Velocity evolution

The expansion velocity of the ejecta is usually measured from the absorption minima of the P Cygni profile by fitting a Gaussian. We choose the relatively isolated lines of H α, H β, He I 5876 Å, Fe II 5169 Å, Ca H & K, and the Ca II NIR triplet. We choose 3934 Å as the rest wavelength for Ca II doublet and 8498 Å for the Ca II NIR triplet. The evolution of the line velocities is shown in Fig. 17. The H α line velocity is about 11 300 km s^{-1} at 11 d after explosion, and fades to ∼8000 km s^{-1} at 80 d after explosion, becoming almost constant thereafter. However, the late-time velocity estimates are affected by a large uncertainty, as the blue wing of the absorption profile of H α is contaminated by the [O I] emission feature. The velocity of Ca II H & K at day 11 is 10 100 km s^{-1}, but has a faster decline until ∼30 d, to become almost constant later on. The velocity trend of He I is similar to that of H α but with comparatively lower velocities. The measured velocity of He I at ∼11 d post-explosion is 7000 km s^{-1}, drops to 5500 km s^{-1} on day 30 and then remains almost constant. The Ca II NIR feature also has a similar trend starting with a velocity of 8000 km s^{-1}, decreasing fast and becoming constant at 6500 km s^{-1}. H β follows a gradual decline with an initial velocity of 8200 km s^{-1} and becomes constant at ∼7000 km s^{-1} around 77 d post-explosion. Fe II lines are considered a good tracer for the photospheric velocity. The Fe II line in SN 2015as has a velocity of 7900 km s^{-1}, and declines to 4200 km s^{-1} at 45 d post-explosion. Mazzali et al. (2009) performed detailed spectral modelling of SN 2003bg in both photospheric and nebular phases revealing the existence of the stratified layers of weaker Balmer lines at 10 000 km s^{-1} followed by He I lines at 7000 km s^{-1}. Similarly, it appears that SN 2015as has a three-layer velocity stratification – an outer layer of H moving with high velocity (∼8000 km s^{-1}); an intermediate Ca-rich layer (7000 km s^{-1}) and a final dense iron core with 4000 km s^{-1}. This scenario can be claimed both from the minima of the absorption profiles that are evolving with time and also from the velocities obtained from the SYN++ modelling. SN 2011dh also showed a similar velocity profile (Sahu et al. 2013), although the velocities in SN 2011dh were slightly higher than in SN 2015as. It is also important to note that not only stratification but optical depth also plays a vital role in this division of velocities.

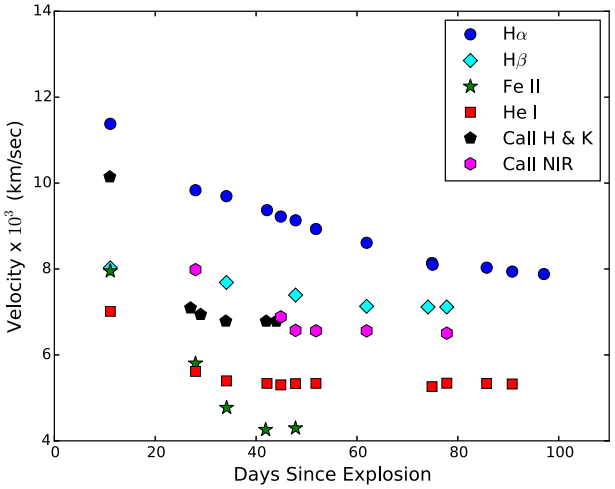

Figure 17. The evolution of the expansion velocity of the SN 2015as ejecta measured from different lines.

In Fig. 18, we compare the velocity evolution of SN 2015as with those of SNe 1993J, 2003bg, 2008ax, 2010as, 2011dh, 2011ei, 2011fu, and 2013df. In the present Type IIb sample, SN 2015as has the lowest observed velocities. At about 10 d after explosion, the H α velocity for other SNe IIb like 2003bg, 2010as, and 2011fu is 17 000 km s^{-1}, while SNe 1993J, 2008ax, 2011dh, and 2013df is ∼13 000 km s^{-1}, which are about 17–18 per cent higher than that of SN 2015as, while SN 2011ei has a similar velocity of 12 500 km s^{-1} (see above; and top-left panel of Fig. 18). Even though H β and He I starts with a lower velocity, a similar trend is also observed for the H β (top-right in the figure) and the He I lines (bottom-left), while Fe II follows a behaviour similar to other SNe IIb (bottom-right). In SN 2015as, H α remained visible for a longer

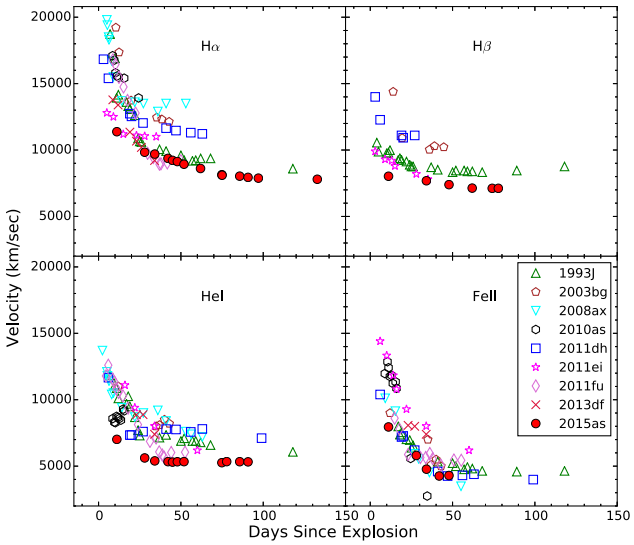

Figure 18. Evolution of line expansion velocities of SN 2015as and a Type IIb SN sample. SN 2015as has the lowest velocity among the comparison sample.

time at lower velocities than all the members of the comparison sample. Iwamoto et al. (1997) showed that the minimum H velocity in SNe IIb mostly depends on the mass of the H envelope retained at the explosion time. For different SNe, the hydrogen mass retained is of the orders of 0.1–0.9 $M_\odot$ for SN 1993J, 0.06 $M_\odot$ for SN 2008ax and 0.1 $M_\odot$ for SN 2011dh (Matheson et al. 2000b; Bersten et al. 2012; Folatelli et al. 2015). The SNe in the comparison sample have comparable H mass and similar explosion energy still SN 2015as has lower expansion velocity than other SNe. This indicates that in the case of SN 2015as, the SN ejecta has higher density. A significant fraction of the explosion energy of SN 2015as is used in expanding the ejecta, leading to lower velocity of the expanding ejecta. Indeed, our observations indicate a peak magnitude towards the faint end of the Type IIb SNe sample distribution, although it is brighter than the faintest SNe 2011ei and 2011hs.

6 CONCLUSION

In this paper, we present comprehensive *BVRIugriz* optical photometric and low-resolution spectroscopic monitoring of the Type IIb SN 2015as. Our photometric observing campaign started 3 d after the explosion and lasted over 500 d, while the spectroscopic observations lasted about 230 d. The colour evolution of SN 2015as has a remarkable resemblance to SN 2008ax, indicating that SN 2015as probably belongs to the subclass of SNe IIb without an early light-curve peak. With a peak V magnitude of -16.82, SN 2015as is brighter than SNe 1996cb, 2011ei and comparable with SN 2011hs. The early-time decay rate of SN 2015as in B band closely matches that of SN 2011dh whereas it is slower than SN 2011fu. The V-band decline of SN 2015as is faster than SNe 2011dh and 2011fu, whereas the R-band and the I-band decay rates of SN 2015as are slower than SNe 2011dh and 2011fu and are faster than SN 1993J. The late-time light-curve evolution of SN 2015as is slower than those of other SNe IIb.

The comparison among quasi-bolometric light curves of SNe IIb shows that SN 2015as is one of the faintest events in our sample. In fact, the brightest object, SN 2011fu, has a peak luminosity of 5.2×10^{42} erg s^{-1}, whereas SN 2015as has a maximum luminosity a factor 3.5 lower (1.5×10^{42} erg s^{-1}). Using the formulation from Arnett (1982), we estimate for SN 2015as $M_{\rm Ni} = 0.08\ M_\odot$, $E_k = 0.65 \times 10^{51}$ erg and $M_{ej} = 2.2\ M_\odot$. The semi-analytical model of Nagy & Vinkó (2016), gives $M_{\rm Ni} = 0.08\ M_\odot$, $E_k = 1.0 \times 10^{51}$ erg, and M_{ej} between 1.1 and 2.2 $M_\odot$. The ^{56}Ni and ejecta masses of SN 2015as are similar to that of SN 2008ax, with a comparatively lower energy budget. The two-component model yields the progenitor radius of SN 2015as ($\sim 0.05 \times 10^{13}$ cm), smaller than those of SN 1993J ($\sim 1.9 \times 10^{13}$ cm; Bersten et al. 2012), SN 2011fu ($\sim 0.3 \times 10^{13}$ cm; Morales-Garoffolo et al. 2015) but comparable with SN 2008ax ($\sim 0.03 \times 10^{13}$ cm; Folatelli et al. 2015).

The early spectra of SN 2015as (until 75 d post-explosion) show prominent Balmer lines, and are similar to those of SNe 1993J and 2011dh while the nebular phase spectra resemble those of SNe 1996cb and 2008ax. The photospheric velocity obtained from the pre-maximum synthetic spectrum, generated by SYN++ was found to be 8500 km s^{-1}. The photospheric velocities of the different lines in SN 2015as are found to be the lowest in the SN sample. The H α line was persistent for a long time in SN 2015as, which indicates that SN 2015as has more residual mass and a much slower dilution of the H envelope than other SNe IIb. Since the ejecta in SN 2015as has a higher density, a significant fraction of the explosion energy is used in expanding the ejecta which results in lower expansion velocity (as seen in SN 2015as) and also a fainter primary peak. The asymmetric profiles of [O I] 6300, 6364 Å in the 132 d spectrum are well explained by the geometry of the emitting region. The minimum ejected mass of O ($\sim 0.45\ M_\odot$), estimated using the [O I] 6300, 6364 line flux, together with the information inferred from the [Ca II] 7291, 7324/[O I] 6300, 6364 line ratio, suggest either a main-sequence progenitor mass of $\sim 15\ M_\odot$ with a He core of 4 $M_\odot$ or a Wolf–Rayet star of 20–25 $M_\odot$ mass like SN 2003bg.

ACKNOWLEDGEMENTS

We sincerely thank the anonymous referee for giving his/her valuable comments and suggestions and carefully going through the manuscript which has significantly improved the presentation of this work. We thank the observing staff and observing assistants at 104 cm ST, 130 cm DFOT, 182 cm EKAR Asiago Telescope, and 200 cm HCT for their support during observations of SN 2015as. SBP and KM acknowledges BRICS grant DST/IMRCD/BRICS/Pilotcall/ProFCheap/2017(G) for the present work. This research has made use of the NASA/IPAC Extragalactic Database (NED) which isoperated by the Jet Propulsion Laboratory, California Institute of Technology, under contract with the National Aeronautics and Space Administration. We acknowledge Wiezmann Interactive Supernova data REPository http://wiserep.weizmann.ac.il (WISeREP) (Yaron & Gal-Yam 2012). This research has made use of the CfA Supernova Archive, which is funded in part by the National Science Foundation through grant AST 0907903. AP, LT, and SB are partially supported by the PRIN-INAF 2014 with the project 'Transient Universe: Unveiling New Types of Stellar Explosions with PESSTO'. The work made use of the SOUSA. SOUSA is supported by NASA's Astrophysics Data Analysis Program through grant NNX13AF35G. BK acknowledges the Science and Engineering Research Board (SERB) under the Department of Science & Technology, Government of India, for financial assistance in the form of National Post-Doctoral Fellowship (Ref. no. PDF/2016/001563).

REFERENCES

Aldering G., Humphreys R. M., Richmond M., 1994, AJ, 107, 662
Anupama G. C., Sahu D. K., Deng J., Nomoto K., Tominaga N., Tanaka M., Mazzali P. A., Prabhu T. P., 2005, ApJ, 631, L125

Arcavi I. et al., 2011, ApJ, 742, L18
Arnett W. D., 1982, ApJ, 253, 785
Arnett W. D., Fu A., 1989, ApJ, 340, 396
Barbon R., Benetti S., Cappellaro E., Patat F., Turatto M., Iijima T., 1995, A&AS, 110, 513
Baron E., Hauschildt P. H., Branch D., 1994, ApJ, 426, 334
Begelman M. C., Sarazin C. L., 1986, ApJ, 302, L59
Ben-Ami S. et al., 2015, ApJ, 803, 40
Bersten M. C. et al., 2012, ApJ, 757, 31
Bessell M. S., Castelli F., Plez B., 1998, A&A, 333, 231
Blondin S., Tonry J. L., 2011, Astrophysics Source Code Library, record ascl:1107.001
Bottinelli L., Gouguenheim L., Paturel G., de Vaucouleurs G., 1985, A&AS, 59, 43
Branch D. et al., 2002, ApJ, 566, 1005
Brown P. J., Breeveld A. A., Holland S., Kuin P., Pritchard T., 2014, Ap&SS, 354, 89
Bufano F. et al., 2014, MNRAS, 439, 1807
Burger J. J., Stephens S. A., Swanenburg B. N., 1970, Ap&SS, 8, 20
Cano Z., 2013, MNRAS, 434, 1098
Chevalier R. A., 1992, ApJ, 394, 599
Chevalier R. A., Soderberg A. M., 2010, ApJ, 711, L40
Chornock R. et al., 2011, ApJ, 739, 41
Colgate S. A., 1970, Ap&SS, 8, 457
Crockett R. M. et al., 2008, MNRAS, 391, L5
de Vaucouleurs G., de Vaucouleurs A., Corwin H. G., Jr, Buta R. J., Paturel G., Fouqué P., 1991, Third Reference Catalogue of Bright Galaxies. Volume I: Explanations and references. Volume II: Data for galaxies between 0^h and 12^h. Volume III: Data for galaxies between 12^h and 24^h. Springer, New York
Deng J., Qiu Y., Hu J., 2001, preprint (arXiv Astrophysics e-prints)
Drake A. J. et al., 2009, ApJ, 696, 870
Drout M. R. et al., 2011, ApJ, 741, 97
Eisenstein D. J. et al., 2011, AJ, 142, 72
Elmhamdi A., Danziger I. J., Cappellaro E., Della Valle M., Gouiffes C., Phillips M. M., Turatto M., 2004, A&A, 426, 963
Elmhamdi A., Danziger I. J., Branch D., Leibundgut B., Baron E., Kirshner R. P., 2006, A&A, 450, 305
Ergon M. et al., 2015, A&A, 580, A142
Filippenko A. V., 1988, AJ, 96, 1941
Filippenko A. V., Matheson T., 2003, preprint (arXiv Astrophysics e-prints)
Filippenko A. V., Sargent W. L. W., 1989, ApJ, 345, L43
Filippenko A. V., Matheson T., Ho L. C., 1993, ApJ, 415, L103
Folatelli G. et al., 2014a, ApJ, 792, 7
Folatelli G. et al., 2014b, ApJ, 793, L22
Folatelli G., Bersten M. C., Kuncarayakti H., Benvenuto O. G., Maeda K., Nomoto K., 2015, ApJ, 811, 147
Fransson C., Chevalier R. A., 1989, ApJ, 343, 323
Fransson C. et al., 2002, ApJ, 572, 350
Fraser M. et al., 2013, ApJ, 779, L8
Fukugita M., Ichikawa T., Gunn J. E., Doi M., Shimasaku K., Schneider D. P., 1996, AJ, 111, 1748
Gehrels N., 2004a, in APS Meeting Abstracts.
Gehrels N., 2004b, in Fenimore E., Galassi M., eds, AIP Conf. Ser. Vol. 727, Gamma-Ray Bursts: 30 Years of Discovery. Am. Inst. Phys., New York, p. 637
Hamuy M. et al., 2009, ApJ, 703, 1612
Harris D. H., 1973, in Greenberg J. M., van de Hulst H. C., eds, IAU Symp. Vol. 52, Interstellar Dust and Related Topics. Springer International Publishing AG., Part of Springer Nature, p. 31
Harutyunyan A. H. et al., 2008, A&A, 488, 383
Houck J. C., Fransson C., 1996, ApJ, 456, 811
Humphreys R. M., Davidson K., Jones T. J., Pogge R. W., Grammer S. H., Prieto J. L., Pritchard T. A., 2012, ApJ, 760, 93
Iwamoto K., Young T. R., Nakasato N., Shigeyama T., Nomoto K., Hachisu I., Saio H., 1997, ApJ, 477, 865
Jeffery D. J., 1990, ApJ, 352, 267
Jerkstrand A., 2017, preprint (arXiv:1702.06702)
Jerkstrand A., Ergon M., Smartt S. J., Fransson C., Sollerman J., Taubenberger S., Bersten M., Spyromilio J., 2015, A&A, 573, A12
Kamble A. et al., 2016, ApJ, 818, 111
Kifonidis K., Plewa T., Scheck L., Janka H.-T., Müller E., 2006, A&A, 453, 661
Kotak R., Vink J. S., 2006, A&A, 460, L5
Krause O., Birkmann S. M., Usuda T., Hattori T., Goto M., Rieke G. H., Misselt K. A., 2008, Science, 320, 1195
Kumar B. et al., 2013, MNRAS, 431, 308
Kuncarayakti H. et al., 2015, A&A, 579, A95
Landolt A. U., 1992, AJ, 104, 340
Leibundgut B., Kirshner R. P., Pinto P. A., Rupen M. P., Smith R. C., Gunn J. E., Schneider D. P., 1991, ApJ, 372, 531
Lewis J. R. et al., 1994, MNRAS, 266, L27
Li H., McCray R., Sunyaev R. A., 1993, ApJ, 419, 824
Li W. et al., 2011, MNRAS, 412, 1441
Liu Y.-Q., Modjaz M., 2017, ApJ, 845, 85
Maeda K., Nomoto K., Mazzali P. A., Deng J., 2006a, ApJ, 640, 854
Maeda K., Mazzali P. A., Nomoto K., 2006b, ApJ, 645, 1331
Maeda K. et al., 2007, ApJ, 666, 1069
Matheson T. et al., 2000a, AJ, 120, 1487
Matheson T., Filippenko A. V., Ho L. C., Barth A. J., Leonard D. C., 2000b, AJ, 120, 1499
Mauerhan J. C. et al., 2013, MNRAS, 431, 2599
Maund J. R., Smartt S. J., 2009, Science, 324, 486
Maund J. R., Wheeler J. C., Patat F., Wang L., Baade D., Höflich P. A., 2007, ApJ, 671, 1944
Maund J. R. et al., 2011, ApJ, 739, L37
Maund J. R. et al., 2015, MNRAS, 454, 2580
Maurer I., Mazzali P. A., Taubenberger S., Hachinger S., 2010, MNRAS, 409, 1441
Mazzali P. A., Nomoto K., Patat F., Maeda K., 2001, ApJ, 559, 1047
Mazzali P. A., Deng J., Hamuy M., Nomoto K., 2009, ApJ, 703, 1624
Milisavljevic D., Fesen R. A., Gerardy C. L., Kirshner R. P., Challis P., 2010, ApJ, 709, 1343
Milisavljevic D. et al., 2013, ApJ, 767, 71
Modjaz M. et al., 2014, AJ, 147, 99
Morales-Garoffolo A., 2016, PhD thesis, Institut de Ciències de l'Espai (CSIC-IEEC)
Morales-Garoffolo A. et al., 2014, MNRAS, 445, 1647
Morales-Garoffolo A. et al., 2015, MNRAS, 454, 95
Mould J. R. et al., 2000, ApJ, 529, 786
Nagy A. P., Vinkó J., 2016, A&A, 589, A53
Nagy A. P., Ordasi A., Vinkó J., Wheeler J. C., 2014, A&A, 571, A77
Nomoto K., Tominaga N., Umeda H., Kobayashi C., Maeda K., 2006, Nucl. Phys. A, 777, 424
Oates S. R. et al., 2012, MNRAS, 424, 1297
Parrent J. et al., 2007, PASP, 119, 135
Parrent J. T., Milisavljevic D., Soderberg A. M., Parthasarathy M., 2016, ApJ, 820, 75
Pastorello A. et al., 2008, MNRAS, 389, 955
Prabhu T. P., Anupama G. C., 2010, in Ojha D. K., ed., ASI Conf. Ser. Vol. 1, Interstellar Matter and Star Formation: A Multi-wavelength Perspective. BASI, p. 193
Prentice S. J. et al., 2016, MNRAS, 458, 2973
Qiu Y., Li W., Qiao Q., Hu J., 1999, AJ, 117, 736
Richardson D., Branch D., Baron E., 2006, AJ, 131, 2233
Richmond M. W., Treffers R. R., Filippenko A. V., Paik Y., Leibundgut B., Schulman E., Cox C. V., 1994, AJ, 107, 1022
Richmond M. W., Treffers R. R., Filippenko A. V., Paik Y., 1996, AJ, 112, 732
Romero-Cañizales C. et al., 2014, MNRAS, 440, 1067
Roming P. W. A. et al., 2005, Space Sci. Rev., 120, 95
Roming P. W. A. et al., 2012, ApJ, 751, 92
Ryder S. D., Sadler E. M., Subrahmanyan R., Weiler K. W., Panagia N., Stockdale C., 2004, MNRAS, 349, 1093
Ryder S. D., Murrowood C. E., Stathakis R. A., 2006, MNRAS, 369, L32

Sagar R., 1999, Curr. Sci., 77, 643
Sagar R., Kumar B., Omar A., Pandey A. K., 2012, in Stepp L. M., Gilmozzi R., Hall H. J., eds, Proc. SPIE Vol. 8444, Ground-based and Airborne Telescopes IV. SPIE, Bellingham, p. 84441T
Sahu D. K., Anupama G. C., Chakradhari N. K., 2013, MNRAS, 433, 2
Scheck L., Plewa T., Janka H.-T., Kifonidis K., Müller E., 2004, Phys. Rev. Lett., 92, 011103
Schlafly E. F., Finkbeiner D. P., 2011, ApJ, 737, 103
Schlegel E. M., Kirshner R. P., 1989, AJ, 98, 577
Schmidt B. P. et al., 1993, Nature, 364, 600
Shivvers I. et al., 2017, PASP, 129, 054201
Silverman J. M., Mazzali P., Chornock R., Filippenko A. V., Clocchiatti A., Phillips M. M., Ganeshalingam M., Foley R. J., 2009, PASP, 121, 689
Sobolev V. V., 1957, Sov. Astron., 1, 678
Sollerman J., Leibundgut B., Spyromilio J., 1998, A&A, 337, 207
Stalin C. S., Hegde M., Sahu D. K., Parihar P. S., Anupama G. C., Bhatt B. C., Prabhu T. P., 2008, Bull. Astron. Soc. India, 36, 111
Stetson P. B., 1992, J. R. Astron. Soc. Can., 86, 71
Stritzinger M., Leibundgut B., 2005, A&A, 431, 423
Stritzinger M. et al., 2009, ApJ, 696, 713
Tartaglia L. et al., 2015, Astron. Telegram, 8291
Taubenberger S. et al., 2009, MNRAS, 397, 677
Taubenberger S. et al., 2011, MNRAS, 413, 2140
Taubenberger S., Kromer M., Pakmor R., Pignata G., Maeda K., Hachinger S., Leibundgut B., Hillebrandt W., 2013, ApJ, 775, L43
Thielemann F.-K., Nomoto K., Hashimoto M.-A., 1996, ApJ, 460, 408
Thomas R. C., Nugent P. E., Meza J. C., 2011, PASP, 123, 237
Tully R. B., Fisher J. R., 1988, Catalog of Nearby Galaxies. Cambridge Univ. Press, Cambridge
Uomoto A., 1986, ApJ, 310, L35
Van Dyk S. D. et al., 2011, ApJ, 741, L28
Van Dyk S. D. et al., 2013, ApJ, 772, L32
Van Dyk S. D. et al., 2014, AJ, 147, 37
Yaron O., Gal-Yam A., 2012, PASP, 124, 668
Zhang Q., Hu J. Y., Wang L. F., Mazzali P. A., Wang Z. R., 1995, MNRAS, 277, 1115

This paper has been typeset from a TEX/LATEX file prepared by the author.